



# Oligopeptide modified ICG/Cisplatin@CaCO<sub>3</sub> for targeted osteosarcoma NIR-II imaging guided multimodal therapy



Li-chen Ji <sup>a,b,c,d,1</sup>, Jia-qing Huang <sup>e,1</sup>, Xu-gang Zhong <sup>a,1</sup>, Long-cai Liu <sup>f</sup>, Qi-hong Sun <sup>g</sup>, Yong Fan <sup>a</sup>, Li Yin <sup>a</sup>, Qing Bi <sup>a</sup>, Qiong Zhang <sup>h,\*</sup>, Yu Cai <sup>f,i,\*</sup>, Ze-ju He <sup>a,\*</sup>

<sup>a</sup> Center for Rehabilitation Medicine, Department of Orthopedics, Zhejiang Provincial People's Hospital (Affiliated People's Hospital), Hangzhou Medical College, Hangzhou, Zhejiang, 310014, China

<sup>b</sup> Department of Joint Surgery, Shanghai East Hospital, School of Medicine, Tongji University, Shanghai, 200092, China

<sup>c</sup> Shanghai Institute of Stem Cell Research and Clinical Translation, Shanghai 200120, China

<sup>d</sup> Shanghai Clinical Research Center for Aging and Medicine, Shanghai, 200040, China

<sup>e</sup> The Fourth Clinic Medical College, Zhejiang Chinese Medicine University, Hangzhou, 310053, China

<sup>f</sup> Clinical Research Institute, Zhejiang Provincial People's Hospital (Affiliated People's Hospital), Hangzhou Medical College, Hangzhou, Zhejiang, 310014, China

<sup>g</sup> Department of Nursing, Zhejiang Provincial People's Hospital, Affiliated People's Hospital, Hangzhou Medical College, Hangzhou, Zhejiang, 310014, China

<sup>h</sup> Center for Operating Room, Department of Nursing, Zhejiang Provincial People's Hospital (Affiliated People's Hospital), Hangzhou Medical College, Hangzhou, Zhejiang, 310014, China

<sup>1</sup> Center for Rehabilitation Medicine, Rehabilitation & Sports Medicine Research Institute of Zhejiang Province, Department of Rehabilitation Medicine, Cancer Center, Zhejiang Provincial People's Hospital (Affiliated People's Hospital), Hangzhou Medical College, Hangzhou, Zhejiang, 310014, China

## ARTICLE INFO

### Keywords:

Phototherapy  
Chemotherapy  
Osteosarcoma  
Targeted therapy

## ABSTRACT

Osteosarcoma, as the most prevalent primary malignant bone tumor, has consistently shown suboptimal clinical treatment outcomes. In this manuscript, we proposed an efficacious and novel phototherapy strategy for osteosarcoma based on a photoresponsive near-infrared (NIR) material, CaCO<sub>3</sub>-ICG-DDP-PEG-PT (CIDP-PT), which contained calcium carbonate (CaCO<sub>3</sub>) and Cisplatin (DDP) via the gas dispersion method, and indocyanine green (ICG) was encapsulated through a nanoprecipitation reaction by employing DSPE-PEG<sub>2000</sub>-COOH to enhance the stability and hydrophilicity. The targeting oligopeptide (PT) for osteosarcoma cells was inserted into the outer membrane of nanoparticles, thereby further enhancing the tumor-targeting capability through receptor-mediated binding. The prepared CIDP-PT nanoparticles exhibited high targeting efficiency and multifunctionality. In vitro and *in vivo* experiments demonstrated that CIDP-PT significantly enhanced the therapeutic efficacy for osteosarcoma via the NIR-II photoresponsive and tumor-targeting approach. It achieves efficient tumor cell eradication through multiple modalities while maintaining an exceptional level of biocompatibility. Hence, the CIDP-PT nanocarriers possess considerable practical value for future clinical applications in adjunct osteosarcoma phototherapy.

## 1. Introduction

Osteosarcoma originates from primitive osteogenic mesenchymal cells, representing one of the most common primary bone tumors [1–4]. It predominantly affects adolescents and exhibits a second peak incidence in males over the age of 50, particularly in the presence of bone deformities such as Paget's disease [5,6]. This highly malignant tumor has a propensity for early metastasis. Pulmonary metastases are

frequently observed, with approximately 10 % to 20 % of diagnosed patients also presenting with metastatic lesions. Within one year of metastasis, pulmonary symptoms can manifest in the absence of chemotherapy, and the five-year survival rate remains below 20 % [7]. Currently, the primary treatment approach for osteosarcoma involves neoadjuvant chemotherapy (preoperative), followed by surgical resection and adjuvant chemotherapy (postoperative) [8,9]. However, the characteristics of osteosarcoma, including its vascularity, invasive

\* Corresponding authors at: Clinical Research Institute, Zhejiang Provincial People's Hospital (Affiliated People's Hospital), Hangzhou Medical College, Hangzhou, Zhejiang 310014, China (Y. Cai).

E-mail addresses: [zqzsrmmyy@163.com](mailto:zqzsrmmyy@163.com) (Q. Zhang), [caiyu@hmc.edu.cn](mailto:caiyu@hmc.edu.cn) (Y. Cai), [Zejuhe@126.com](mailto:Zejuhe@126.com) (Z.-j. He).

<sup>1</sup> Li-chen Ji, Jia-qing Huang, Xu-gang Zhong have contributed equally to this work.

<https://doi.org/10.1016/j.mateds.2024.112965>

Received 21 November 2023; Received in revised form 19 March 2024; Accepted 20 April 2024

Available online 21 April 2024

0264-1275/© 2024 The Authors. Published by Elsevier Ltd. This is an open access article under the CC BY-NC license (<http://creativecommons.org/licenses/by-nc/4.0/>).

growth, and close adherence to surrounding tissues, often pose challenges in achieving precise tumor margin resection and complete eradication of tumor cells through surgery. Furthermore, chemotherapy alone cannot fully address the issues of primary tumor progression and metastasis [10,11]. As a result, the diagnosis and treatment of osteosarcoma have encountered limitations over the past three decades [12,13]. Moreover, surgical procedures and chemotherapy, while producing clinical efficacy, give rise to significant negative impacts on patients' quality of life. These include limb pain, impaired mobility, bone marrow suppression, gastrointestinal reactions, and cytotoxic effects on healthy cells [3,14]. Therefore, inhibiting the growth of osteosarcoma, preventing recurrence and metastasis, enhancing the effectiveness of chemotherapy, and reducing adverse reactions remain urgent challenges that need to be addressed [15].

Phototherapy is a novel clinical treatment method that involves exposing the affected area of the patient to a light source, utilizing transformative energy or triggering chemical reactions to achieve the eradication of diseased tissue cells while minimizing damage to normal tissue cells [16–18]. Due to its non-invasive nature and ease of operation, phototherapy utilizing various artificial light sources has been widely introduced in the research and treatment of diseases beyond dermatological conditions. Previous studies have demonstrated significant tumor eradication effects of phototherapy in malignancies such as primary or metastatic liver cancer, colorectal cancer, bladder cancer, breast cancer, glioblastoma, and renal cancer, reducing the likelihood of recurrence and metastasis [19]. Furthermore, by adjusting the type, wavelength, and power of the light source, complications can be controlled to a milder extent [20–23]. Over the years, tumor phototherapy has evolved into two forms of treatment. Photothermal therapy (PTT) refers to the conversion of light energy into heat energy using photothermal conversion agents, leading to thermal destruction of tumors. Photodynamic therapy (PDT), on the other hand, involves the use of specific photosensitizers that, under irradiation from a specific wavelength light source, undergo an activated reaction generating various reactive oxygen species (e.g., hydrogen peroxide, singlet oxygen, superoxide anion radicals, hydroxyl radicals) to induce photodynamic oxidative damage to tumor cells at the site of the lesion. This is achieved by disrupting the cellular structures of tumor cells, such as the cell membrane, mitochondria, and lysosomes, resulting in their eradication [24]. The light sources for phototherapy have evolved from simple sunlight, filtered sunlight, and carbon arc-ultraviolet to encompass a variety of light sources, including near-infrared light. Notably, near-infrared (NIR) light has gained significant attention in current research due to its high tissue penetration and low absorption by biomolecules, making it a popular choice for tumor phototherapy. These advancements not only improve the effectiveness of phototherapy but also minimize damage to surrounding normal tissue. Furthermore, the low toxicity, high specificity, high sensitivity, and reduced likelihood of resistance make phototherapy highly promising in its utilization.

However, as the clinical application progresses, the limitations of phototherapy have gradually become apparent. Inorganic photothermal materials, including metal nanomaterials (gold nanocages, Ag nanoparticles, etc.) [25,26], metalloids nanomaterials (Bi nanoparticles, Silicon nanocrystals, etc.) [27,28] and metal oxide nanomaterials ( $ZrO_2$  nanoarrays,  $TiO_2$  Nanoarrays, etc.) [29,30], were once a hot research topic among scientists. However, they encounter issues such as difficulty in degradation and slow metabolism in the body, which can easily cause long-term potential toxicity. Furthermore, apart from conversion efficiency, the biocompatibility and characteristics of biomaterials further restrict the clinical application of photosensitizers. Photosensitizers derived from material polymers also present numerous issues such as high toxicity, high solubility, easy excretion, and poor targeting ability *in vivo*. Therefore, the development or preparation of photosensitizing materials with excellent clinical efficacy holds significant importance in maximizing the therapeutic effects and feasibility of phototherapy for tumors.

ICG is a bipartite cyanine dye that was approved for clinical use by the United States Food and Drug Administration (FDA) in 1954. It has been widely utilized in clinical applications, such as assessing cardiac function and liver function. In the 1970 s, researchers discovered that ICG bound to proteins exhibits strong absorption in the NIR spectrum. Due to the low absorption of biological tissues in the NIR bio-window, ICG can be applied in optical imaging and phototherapy as it offers good energy conversion efficiency and signal-to-noise ratio [31]. The high energy conversion efficiency enables ICG to heat the cellular microenvironment after NIR light irradiation, resulting in localized hyperthermia and the destruction of cancer cells [32]. Additionally, when ICG is used as a photosensitizer exposed to specific wavelength light sources, it possesses the ability to generate significant reactive oxygen species (ROS), including singlet oxygen and superoxide radicals [33]. ROS promotes cancer cell apoptosis through various mechanisms, such as downregulating apoptosis-regulating proteins like caspase-8 inhibitory protein through ubiquitination. It induces intracellular  $Ca^{2+}$  release or influx by acting on phospholipase A2 on the cell membrane. It activates the p38 mitogen-activated protein kinase signaling pathway, thereby participating in Fas-FASL-mediated cell apoptosis. It induces the opening of the mitochondrial permeability transition (MPT) pore, leading to decreased mitochondrial transmembrane potential, release of cytochrome C, and subsequent activation of a series of caspase enzymes, among others. Moreover, ROS can also mediate tumor cell necrosis through the regulation of c-Jun phosphorylation and poly (ADP-ribose) polymerase-1 (PARP-1). Therefore, ICG is considered a promising adjuvant for phototherapy. However, ICG has certain limitations, including concentration-dependent aggregation, short half-life, poor photostability, poor hydrolytic stability, nonspecific binding to proteins, and nonspecific targeting [32], which restrict its further therapeutic and diagnostic applications in cancer treatment. One of the methods to overcome these limitations is incorporating ICG into nanoparticle delivery platforms. Examples of such platforms include calcium-based nanoparticles, lipid-based nanoparticles, polymer-based nanoparticles, magnetic nanoparticles, and mesoporous silica nanoparticles [34,35]. These combinations can enhance the functionality of photosensitizers through complementary material characteristics. Among them, calcium-based nanoparticles, due to their excellent biocompatibility, low toxicity, efficient biodegradability, and targeting ability, have become a mature member of drug delivery systems.  $CaCO_3$ , a widely occurring inorganic material in nature, was selected. It exhibits remarkable biocompatibility and biodegradability, along with good acid sensitivity, which enables its stable existence in a neutral environment and provides protective effects on the encapsulated cargo. In the acidic tumor microenvironment,  $CaCO_3$  can be degraded into  $Ca^{2+}$  and  $CO_2$ .  $Ca^{2+}$  can interact with ROS, further enhancing tumor cell apoptosis and necrosis.

The present study encompasses the synthesis of a novel phototherapy adjunct material, harnessing the exceptional properties of ICG to endow it with efficient NIR light absorption efficiency, energy conversion efficiency, and chemical reaction excitation efficiency, all working collectively to eradicate tumor cells. Furthermore, this material exhibits favorable photothermal stability and aggregation characteristics, thereby minimizing damage to surrounding healthy tissues. To enhance tumor-targeting specificity and multifaceted cytotoxicity within the acidic tumor microenvironment, we employed a calcium-based nano-carrier platform in conjunction with platinum-based chemotherapy to augment the specific anti-osteosarcoma efficacy of the nanomaterial. Additionally, the stability and hydrophilicity of the nanostructures were reinforced by integrating DSPE-PEG<sub>2000</sub>-COOH. Lastly, targeted peptides are well known for their efficient and specific binding to cell ligands. It has the characteristics of easy synthesis, easy chemical modification, low antigen reactivity and high histocompatibility. In addition, targeted peptides are widely used in drugs and delivery systems because of their good physical stability, good pharmacokinetics, low toxicity and easy excretion. Among them, oligopeptide (PT) peptide has become a target substance for the study of osteosarcoma and other

diseases because it mimics the characteristics of natural protein osteocalcin in vivo and has good targeting property. we strategically inserted a tumor-targeting PT into the outer membrane site of osteosarcoma cells [36], further bolstering the tumor-targeting capabilities through receptor-mediated biological binding. The materials targeted to the osteosarcoma environment can exert therapeutic effects through a multi-modal approach involving hyperthermia, ROS production, calcium overload, and direct cytotoxicity induced by chemotherapeutic agents. Considering its convenience, efficacy, and low drug resistance, this approach holds great promise for future osteosarcoma treatment endeavors.

## 2. Material and methods

### 2.1. Materials and characteristics

DSPE-PEG<sub>2000</sub>-COOH was obtained from Ponsure Biotech (Shanghai, China). ICG was purchased from Aladdin (Shanghai, China). C<sub>11</sub>H<sub>13</sub>N<sub>3</sub>O<sub>4</sub> (EDC) and C<sub>4</sub>H<sub>5</sub>NO<sub>3</sub> (NHS) were acquired from Sigma-Aldrich. Cisplatin was obtained from MCE (Shanghai, China). 3-(4,5-dimethylthiazol-2-yl)-2,5-diphenyltetrazolium bromide (MTT) assay kits were purchased from Sangon Biotech (Shanghai, China). Calcium indicator/PI cell viability/cytotoxicity assay kits and DAPI were obtained from Beyotime Biotechnology. Annexin V-FITC apoptosis assay kit was purchased from Li-COR Biosciences (Hangzhou, China). DMEM culture medium was obtained from Gibco (California, USA), and fetal bovine serum was purchased from Gibco (California, USA). The morphology of CIDP-PT was observed using a transmission electron microscope (TEM, HT7700, Hitachi). The size distribution (diameter, nm) and surface charge (zeta potential, mV) of the nanoparticles were measured by the Zetasizer Nano ZS particle analyzer (Malvern Instruments Limited). The UV-vis absorption spectrums of nanoparticles were recorded using a UV-vis spectrophotometer (Thermo Fisher).

### 2.2. Synthesis of CIDP-PT

Carbonate apatite nanoparticles loaded with cisplatin (CaCO<sub>3</sub>-DDP) were prepared using a gas dispersion method. To achieve this, 220 mg of CaCl<sub>2</sub>·6H<sub>2</sub>O and 2 mg of DDP were added to 100 mL of anhydrous ethanol and thoroughly stirred until fully dissolved. The mixture was then covered with tin foil containing small perforations, placed inside a larger drying vessel, and surrounded by four open bottles containing 2 g of dried NH<sub>4</sub>CO<sub>3</sub> and 3.5 g of CuSO<sub>4</sub> solution. Vacuum was applied using a vacuum pump, and the setup was left at room temperature for 24 h. This process resulted in anhydrous ethanol solution of DDP-CaCO<sub>3</sub>, which was dried using a rotary evaporator. Subsequently, 2 mg of DDP-CaCO<sub>3</sub> particles were dissolved in methanol along with 1 mg of ICG, and sonication was employed to promote dissolution. A suitable amount of DSPE-PEG<sub>2000</sub>-COOH was added to the solution, which was then stirred overnight in the absence of light. The resulting mixture was further dried using rotary evaporation, leading to the formation of CaCO<sub>3</sub>-ICG-DDP-PEG (CIDP). The particles were dissolved in deionized water. 10 μL EDC and 0.5 mg NHS were added into pre-prepared CIDP NPs solution and the solution was stirred at room temperature for 2 h. Then the PT peptide solution (1 mg) in water (0.5 mL) was added into the CIDP NPs solution and further stirred for 12 h. The nanoparticles suspension was dialyzed in ddH<sub>2</sub>O for two days (MWCO: 3500). After 48 h of freeze-drying, CIDP-PT particles were obtained (Graphical abstract Hig).

### 2.3. Determination of drug loading efficiency in CIDP-PT

In evaluating CIDP-PT's ability to encapsulate DDP, we utilized the drug loading efficiency (LE%). Loading efficiency generally denotes the percentage of the loaded drug relative to the total mass of the carrier. The calculation formula is outlined as follows:

$$LE\% = \frac{\text{weight of the drug in NPs}}{\text{weight of the feeding nanocarrier and the drug}}$$

We employed inductively coupled plasma mass spectrometry (ICP-MS) to measure the DDP content in CIDP-PT for calculating the drug loading efficiency. Precisely, 4 mg of CIDP-PT was dissolved in 1 mL PBS, and the solution was adjusted to acidity using pH paper. After vortexing for 5 min, the solution underwent a 15-minute ultrasonic treatment in a water bath sonicator. Following filtration through a 0.22 μm membrane, the solution was taken, diluted to 10 mL, and the DDP content was measured. The drug loading efficiency of DDP was then calculated using the aforementioned formula.

### 2.4. In vitro drug release behavior of CIDP-PT

To evaluate the in vitro drug release performance of DDP from the nanoparticles, two identical solutions of CIDP-PT (with a platinum concentration of approximately 1 mg/mL, 5 mL) were prepared. Each solution was placed in a dialysis bag and immersed in 200 mL of pH 7.4 phosphate-buffered saline (PBS) solution and pH 4.5 acetate buffer solution, respectively. The temperature was maintained at 37 °C with constant agitation at 150 rpm, and the experiment was timed. At the time points of 0, 10, 20, 30, 40, and 50 h, 5 mL of the external dialysis solution was withdrawn using a pipette, and an equal volume of the corresponding pH 7.4 and pH 4.5 buffers was replenished. The concentration of DDP in the released medium at each time point was determined by inductively coupled plasma mass spectrometry (ICP-MS). The cumulative release rate (ARR%) of DDP was calculated using the following formula, and in vitro release curves were plotted for pH 7.4 and pH 4.5 conditions.

$$ARB\% = \left( C_i \times V_{solution} + \sum \text{from } 1 \text{ to } i-1 (C_{i-1} \times V_{i-1}) \right) / (C_{drug} \times V_{NPs})$$

where C<sub>i</sub> and C<sub>i-1</sub> represent the concentration of the drug in the current and previous samples (C<sub>0</sub> = 0), V<sub>solution</sub> represents the volume of the release medium, V<sub>i-1</sub> is the volume of the previous sample (V<sub>0</sub> = 0), C<sub>drug</sub> is the concentration of the drug in the nanoparticle solution, and V<sub>NPs</sub> represents the volume of the nanoparticle solution.

### 2.5. Photothermal performance of CIDP-PT

A volume of 1 mL of CIDP-PT solution with different concentrations of ICG (0, 10, 20, 30, 40, 50, 100 μg/mL) was placed under illumination from an 808 nm laser with various power densities (0.5, 1, 1.5, and 2 W/cm<sup>2</sup>) for 600 s. Meanwhile, the temperature of each solution was recorded every 60 s using an infrared imaging thermometer. For further analysis, a 1 mL CIDP-PT solution (ICG concentration of 50 μg/mL) and a 1 mL free ICG control group were exposed to 1.5 W/cm<sup>2</sup> of 808 nm laser for 5 min, followed by natural cooling for 5 min. This process was repeated five times (totaling 50 min), and the solution temperature was recorded every minute using a thermometer. The photothermal performance of CIDP-PT was evaluated based on the temperature changes observed under different conditions.

### 2.6. In vitro dual-modal imaging

A 1 mL volume of CIDP-PT solution with varying concentrations of ICG (0, 0.5, 1, 2, 5, 10, 20, 50, 100 μg/mL), along with corresponding gradients of free ICG at the same concentrations, was placed in a small animal in vivo fluorescence imaging system for photography, followed by fluorescence quantification.

### 2.7. Photodynamic singlet oxygen generation of CIDP-PT

A volume of 1 mL of free ICG and CIDP-PT solutions were separately

mixed with SOSG dye in quartz cuvettes, ensuring that the concentration of SOSG in each solution was 20 µg/mL, with a relative content of 20 µg compared to ICG. The absorbance of the mixtures was measured using a UV-visible spectrophotometer ( $\lambda_{\text{ex}} = 475 \text{ nm}$ ,  $\lambda_{\text{em}} = 530 \text{ nm}$ ). Subsequently, the mixtures were irradiated with an 808 nm laser at a power density of  $1.5 \text{ W/cm}^2$  for 10 min, and the absorbance was scanned every minute. By comparing the spectral changes of each solution, the generation of singlet oxygen by CIDP-PT was characterized.

## 2.8. Cell culture

Osteosarcoma (143B/MG63) cells, breast cancer (MDA-MB-231) cells, and normal lung epithelial cells (BEAS-2B) were obtained from ATCC. They were grown in DMEM culture medium supplemented with 10 % FBS and 1 % penicillin-streptomycin. All cells were cultured in a humidified incubator with 5 % CO<sub>2</sub> concentration, and 90 % relative humidity at 37 °C. Fresh culture medium was replaced 3–4 times per week, and cells were passaged and seeded in cell culture flasks (Corning) according to the recommended guidelines.

## 2.9. Cellular uptake

143B/MG63 cells and MDA-MB-231 cells were seeded at a density of  $1 \times 10^5$  cells/dish in 35 mm diameter, glass-bottom (0.13 mm thickness) cell culture dishes and incubated for 24 h. The culture medium was then replaced with solutions of free ICG, CIDP, and CIDP-PT (with an ICG concentration of 20 µg/mL). The cells were incubated in the dark for 4 h, followed by removal of the culture medium and washing the cells three times with 1 × PBS (pH 7.4). After staining with DAPI (1 µg/mL) for 10 min, the cells were washed again three times with 1 × PBS (pH 7.4). Cellular fluorescence and uptake were observed using a confocal laser scanning microscope (CLSM) (Leica, TCS-SP5). Images were captured for documentation. Fluorescence quantification analysis was performed using ImageJ software.

## 2.10. In vitro cell viability

143B cells were seeded in a 96-well plate at a density of  $5 \times 10^3$  cells/well and cultured for 24 h. Subsequently, the culture medium was replaced with medium containing different concentrations of free ICG, DDP, CIDP, and CIDP-PT, and the cells were incubated in the dark in a cell culture incubator for 12 h. For the groups treated with free ICG, CIDP, and CIDP-PT, the cells were irradiated with an 808 nm laser at a power density of  $1.5 \text{ W/cm}^2$  for 5 min, followed by an additional 12 h of incubation in a CO<sub>2</sub> incubator. The cell viability of each group, either single drug or laser combination, was assessed using the MTT assay. The absorbance of each sample at 570 nm was measured using an ELISA reader to calculate the relative cell viability as the ratio of the sample absorbance to the absorbance of the control group. Furthermore, normal lung epithelial cells (BEAS-2B) were also seeded in a 96-well plate and co-cultured with DDP and CIDP-PT, and the same methods were used to assess the cytotoxicity of DDP and CIDP-PT on human normal organ cells.

## 2.11. Cell apoptosis detection

143B cells were seeded in 6-well plates at a density of  $1 \times 10^6$  cells/well. After treatment with PBS, free ICG, CIP-PT, CIDP, or CIDP-PT (with a controlled ICG concentration of 20 µg/mL) alone or in combination with an 808 nm laser at a power density of  $1.5 \text{ W/cm}^2$ , the cells were digested with trypsin without EDTA and collected by centrifugation. After washing twice with cold PBS and centrifugation, the cell pellets were resuspended in 1 mL binding buffer. Approximately  $5 \times 10^5$  cells from each group were transferred to flow cytometry tubes and stained with Annexin V-FITC/PI staining reagents from the UE Biotechnology Co. (Watertown, USA) in the dark on ice. The percentage of apoptotic

cells was immediately determined using a flow cytometer (Becton Dickinson and Co., Franklin Lakes, NJ, USA).

## 2.12. Western Blot analysis

Total protein was extracted from tissue homogenates or cell lysates using pre-chilled RIPA buffer (Fude Biotechnology, China) supplemented with protease inhibitors (Fude Biotechnology, China). The protein samples were diluted to equal concentrations, denatured in a metal bath, separated by SDS-PAGE, and transferred onto a polyvinylidene difluoride (PVDF) membrane (Merck Millipore, Germany). Electrophoresis was performed in a 10 % polyacrylamide gel, followed by transfer to a polyvinylidene difluoride (PVDF) membrane (Millipore, Burlington, MA, USA). The membrane was blocked with 5 % non-fat milk in TBST buffer and then incubated with the primary antibody at 4 °C overnight. After washing the membrane four times with TBST buffer, it was incubated with a secondary antibody conjugated to horseradish peroxidase (HRP) for 120 min at 25 °C. Protein bands were visualized using a chemiluminescence imaging system (Bio-Rad, USA).

## 2.13. Calcein-AM / PI staining assay

143B cells were seeded in 35 mm glass-bottom cell culture dishes with a thickness of 0.13 mm and incubated for 12 h. The cells were then treated with equal volumes of PBS (control group), free-ICG, CIP-PT, CIDP, and CIDP-PT (ICG concentration of 20 µg/mL) in DMEM without FBS, respectively, for two groups of cells. One group of cell culture dishes was subjected to 5 min of laser irradiation using an 808 nm laser at a power density of  $1.5 \text{ W/cm}^2$  and then incubated for an additional 24 h. Afterwards, all cell groups were washed with PBS three times, fixed with 4 % paraformaldehyde solution, and stained with Calcein-AM / PI live/dead cell reagent. The cells were washed with PBS again. Confocal laser scanning microscopy (TCS SP5; Leica Microsystems, Bannockburn, IL, USA) was used to capture images of the live/dead cell staining pattern.

## 2.14. Detection of light-induced ROS in 143B cells with CIDP-PT

143B cells were seeded in 35 mm glass-bottom cell culture dishes with a thickness of 0.13 mm at a density of  $1 \times 10^5$  cells per dish and incubated for 24 h. After removing the culture medium, free-ICG and CIDP-PT (ICG concentration of 20 µg/mL) were added to the respective groups. The ROS detection reagent, DCFH-DA, from a commercial kit (Beyotime Biotechnology, China), was added to the different groups of cell culture dishes. The cells were irradiated with an 808 nm laser (light intensity:  $1.5 \text{ W/cm}^2$ ) for 5 min. Confocal laser scanning microscopy was used to observe the fluorescence in 143B cells and ImageJ software was used for fluorescence quantification analysis. The production of ROS inside 143B cells was evaluated to assess the PDT effect of CIDP-PT.

## 2.15. Cell migration and proliferation assay

To investigate the effect of CIDP-PT on the migratory ability of osteosarcoma cells, 143B cells were seeded in 6-well plates ( $5 \times 10^6$  cells per well) until reaching 80–90 % confluence. The culture medium was then removed, and PBS (control group), PBS + laser, free-ICG + laser, CIDP + laser, CIDP-PT, and CIDP-PT + laser (ICG concentration of 20 µg/mL) were processed separately for co-incubation for 12 h. The cells were scratched using a pipette tip and cultured in serum-free medium for 24 h. Cell migration images were obtained at 0, 6, 12, and 24 h after scratching.

## 2.16. Transwell assay

The invasive ability of 143B cells was measured using Transwell chambers with an 8.0 µm pore size and coated with matrix gel (BD

Biosciences, Shanghai, China). 143B cells were treated with PBS (control group), ICG, CIP-PT, CIDP, and CIDP-PT as single-drug treatments or combined with laser treatment. Subsequently, 200  $\mu$ L of 143B cells suspended in serum-free DMEM was added to the upper chamber, while 600  $\mu$ L of medium containing 10 % FBS was added to the lower chamber. After 12 h, the invaded 143B cells on the bottom of the membrane were fixed with formaldehyde and stained with 0.1 % crystal violet. Finally, invaded cells were counted in randomly selected areas under a microscope at 40x magnification.

### 2.17. Colony formation assay

143B cells treated with PBS, ICG, CIP-PT, CIDP, and CIDP-PT ( $\pm$ laser) were collected using a 0.25 % trypsin-EDTA solution, centrifuged, and then seeded in 60 mm culture dishes at a density of 1000 cells per well. The dishes were placed under 37 °C and 5 % CO<sub>2</sub> conditions for two weeks of incubation. On the 10th day, all the culture media were removed, and the cells were fixed with 4 % paraformaldehyde for 25–30 min. Subsequently, the colonies were stained with 0.5 % crystal violet for 30 min and counted.

### 2.18. Animal and tumor model

BALB/c nude male mice (5 weeks old, 18–20 g) were used for in vivo studies. 143B cells were digested with trypsin, centrifuged, and resuspended in PBS buffer. The cell suspension concentration was adjusted to  $5 \times 10^6$  cells/mL by counting. The 143B cell suspension was injected subcutaneously into the right hind limb of BALB/c nude male mice at a dose of 200  $\mu$ L per mouse to form the osteosarcoma model. The injection day was recorded as day 0. Tumor volume was calculated using the formula  $V = a^*b^2/2$ , where “a” represents the value of the longest diameter of the tumor and “b” represents the value of the shortest diameter of the tumor. The animal experiment was approved by the Ethics Committee of Zhejiang Provincial People’s Hospital (Approval Number:20230718162204352841).

### 2.19. Distribution experiment of CIDP-PT in nude mice

BALB/c nude male mice were used to establish a 143B mouse osteosarcoma model. Thirty osteosarcoma-bearing nude mice were randomly divided into six groups: PBS group, ICG + laser group, CIP-PT group, CIP-PT + laser group, CIDP-PT group, and CIDP-PT + laser group. Free ICG, CIP-PT, and CIDP-PT solutions were prepared and administered via tail vein injection at a dose of 1.5 mg/kg of ICG. Before imaging, the mice were anesthetized with isoflurane and provided enough oxygen to ensure normal survival. Images were taken using the same parameters on a small animal fluorescence imaging system (BLT AniView 100, Guangzhou Biolight Biotechnology Co., Ltd.) at 0 h, 1 h, 2 h, 4 h, 8 h and 24 h after administration (ICG and CIDP-PT group), and the fluorescence distribution at each time point was collected.

### 2.20. Evaluation of in vivo photothermal effect

To further evaluate the photothermal therapeutic effect of CIDP-PT in vivo, an infrared imaging temperature meter was used to assess the photothermal effect of CIDP-PT in subcutaneous osteosarcoma-bearing nude mice. Six osteosarcoma-bearing nude mice with tumor volumes of 150 mm<sup>3</sup> were randomly divided into two groups and administered PBS or CIDP-PT (at a dose of 1.5 mg/kg ICG) via tail vein injection. After 24 h, the mice were anesthetized with isoflurane, and the tumors of each mouse were exposed to an 808 nm laser (power density: 1 W/cm<sup>2</sup>; irradiation power: 1.5 W; irradiation area: 1.5 cm<sup>2</sup>) for 5 min. The temperature at the tumor site was detected using an infrared imaging temperature meter, and photographs were taken.

### 2.21. In vivo experiments using a xenograft tumor model

Thirty BALB/c nude male mice with subcutaneously implanted tumors with a volume of 150 mm<sup>3</sup> were randomly divided into six groups: PBS group, ICG + laser group, CIP-PT group, CIP-PT + laser group, CIDP-PT group, and CIDP-PT + laser group (5 mice per group). Free-ICG, CIP-PT, and CIDP-PT solutions were administered via tail vein injection. After 24 h, the tumor sites of the mice were irradiated with an 808 nm laser at a power density of 1.5 W/cm<sup>2</sup>. During the treatment period, each group of mice received one drug administration and one light irradiation every 4 days, totaling two administrations. Tumor diameter was measured every two days, and tumor volume (V) was calculated using the formula. A tumor volume versus treatment time curve was plotted. On day 15, the mice in each group were euthanized, and the major organs and tumor tissues were collected. Histopathological sections were prepared and stained with hematoxylin and eosin (H&E) for observation. Blood samples were collected from each group for biochemical and hematological analysis.

### 2.22. Biocompatibility testing

As mentioned above, starting from the day of treatment initiation, the body weight and tumor volume of the mice were monitored and recorded every two days. A weight change curve was plotted to preliminarily evaluate the biocompatibility of CIDP-PT. Blood samples were collected from each group and analyzed using a blood cell analyzer (Sysmex, Japan and Mindray BC-2800vet, China) to measure biochemical parameters and Blood routine parameters. The major organs and tumor tissues of the mice were fixed in 4 % paraformaldehyde for H&E staining. By observing the tissue sections of the major organs of the osteosarcoma-bearing BALB/c nude male mice in each group after treatment, the in vivo safety of CIDP-PT was further evaluated.

### 2.23. Statistical analysis

Data analysis and presentation of results were performed using SPSS (SPSS Inc., Chicago, IL, USA) and GraphPad Prism 8 (GraphPad Software Inc., La Jolla, CA, USA). A significance level of  $p < 0.05$  was considered statistically significant.

## 3. Results

### 3.1. Preparation and characterization of CIDP-PT

Firstly, a gas dispersion method is employed, wherein CO<sub>2</sub> gas generated by the volatilization of NH<sub>4</sub>HCO<sub>3</sub> reacts with Ca<sup>2+</sup> in anhydrous ethanol solution to prepare an acid-sensitive CaCO<sub>3</sub>-DDP nanoparticle. The nanoparticles are rich in drug-carrying channels to encapsulate the photosensitizer ICG to form a CaCO<sub>3</sub>-ICG-DDP (CID) core. DSPE-PEG<sub>2000</sub>-COOH is coated onto its surface to enhance the water solubility and stability of the material. To further enhance targeting to osteosarcoma cells, 1-ethyl-3-(3-dimethylaminopropyl) carbodiimide (EDC)/N-hydroxysuccinimide (NHS) was used to activate the carboxyl groups on the surface of CIDP NPs, and the PT oligopeptide is bonded to the activated carboxyl groups. The morphological characterization of CIDP-PT, as revealed by TEM analysis, demonstrated particle sizes that were consistent with those obtained using dynamic light scattering principles. The particles exhibited a uniform and spherical shape, with no adhesion or aggregation observed between the nanospheres (Fig. 1A). The nanoparticle size and Zeta potential of CIDP-PT were measured using a nanoscale particle size analyzer. The particle size of CIDP-PT was determined to be  $181.73 \pm 5.06$  nm, displaying a homogeneous distribution with a single peak (Fig. 1B). The CIDP-PT particle size was found to be less than 200 nm, meeting the fundamental requirements for passive targeting to tumor tissues through the enhanced permeability and retention (EPR) effect. The surface Zeta

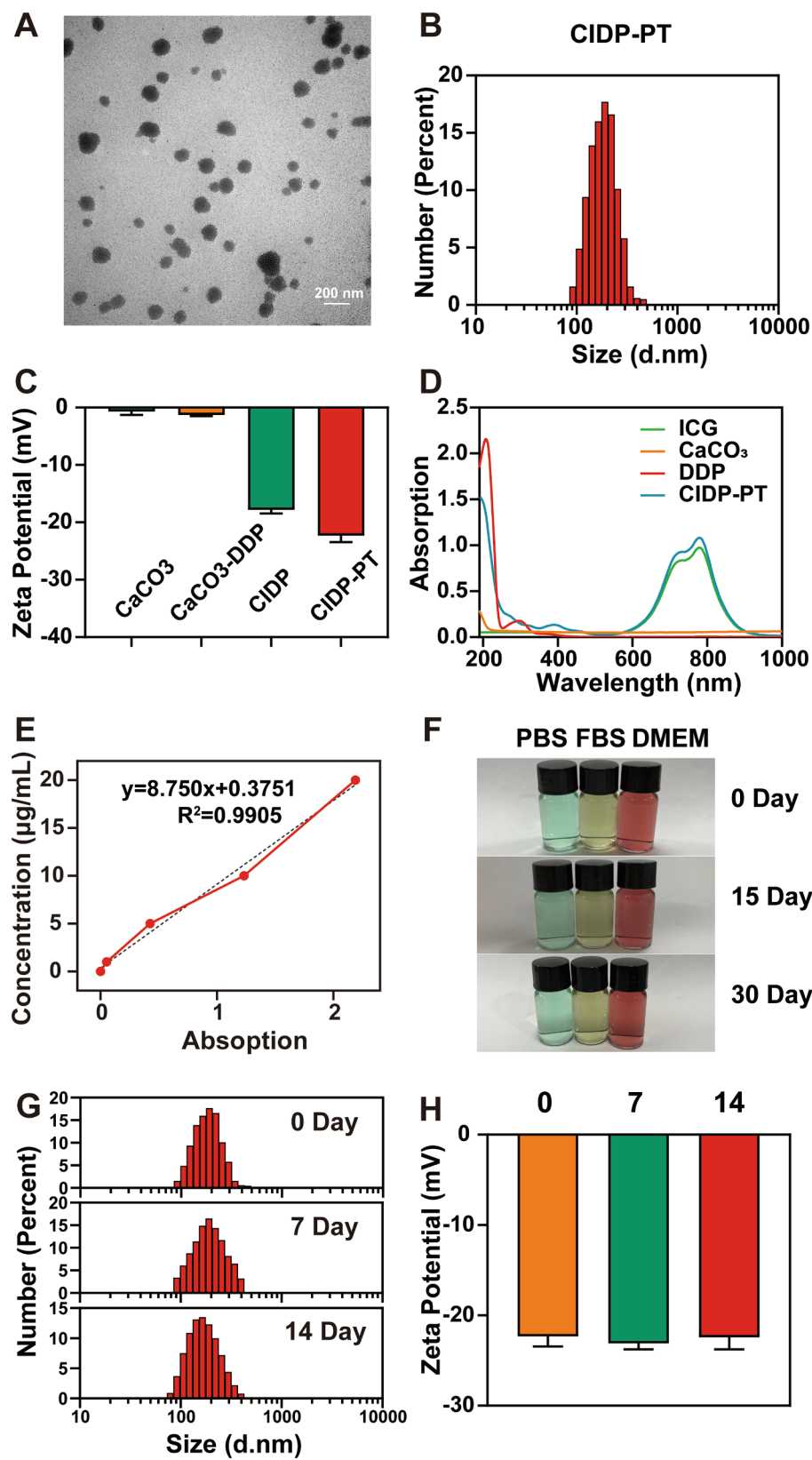


**Fig. 1.** Characterization of CIDP-PT (A) Electron microscopic diagram of CIDP-PT (scale bar = 200 nm); (B) The particle size distribution CIDP-PT; (C) The zeta potential of  $\text{CaCO}_3$ ,  $\text{CaCO}_3$ -DDP, CIDP, and CIDP-PT, the results shown is mean  $\pm$  SD; (D) Ultraviolet absorbance spectrum of CIDP-PT; (E) ICG 780 nm ultraviolet absorbance and concentration standard curve; (F) Suspension stability of CIDP-PT in PBS, FBS and DMEM at 0, 15 and 30 days; (G) Relative particle size distribution changes of CIDP-PT after the store for 0, 7 and 14 days. (H) The surface zeta potential of CIDP-PT after the store for 0, 7 and 14 days. Mean  $\pm$  S.D., n = 3.

potential was measured at  $-22.33 \pm 1.10$  mV, promoting the storage stability of the nanoparticles. The zeta potentials of the intermediate products in the CIDP-PT synthesis process were also measured (Fig. 1C). Additionally, we employed a UV-visible spectrophotometer to obtain UV absorption spectra of different components. The absorption peaks of CIDP-PT were observed at the wavelengths corresponding to ICG, CaCO<sub>3</sub>, and DDP, confirming the successful encapsulation of these key components within the material (Fig. 1D). Furthermore, an absorption-concentration standard curve for ICG was generated at a wavelength of 780 nm, yielding a linear equation of  $y = 8.750x + 0.3751$  with an  $R^2$  value of 0.9905 (Fig. 1E). CIDP-PT, dissolved in PBS, FBS, and DMEM culture media at a concentration of 20  $\mu$ g/mL (standard ICG), exhibited excellent suspension stability in all three solvents and maintained its properties without any observable agglomeration or precipitation after long-term storage (Fig. 1F). Additionally, we measured the particle size (Fig. 1G) and Zeta potential (Fig. 1H) of CIDP-PT in PBS over a two-week period. There were no significant changes observed at 7 and 14 days, further confirming that CIDP-PT does not undergo degradation within this timeframe, thereby preventing drug leakage and potential side effects on non-target tissues during the treatment process.

### 3.2. Material characteristics of CIDP-PT

Regarding the material properties, we initially compared the photothermal effect of CIDP-PT at different concentrations (ICG concentrations of 0, 10, 20, 30, 40, 50, 100  $\mu$ g/mL) under 808 nm irradiation with a power density of 1.5 W/cm<sup>2</sup>. As depicted in Fig. 2A, the CIDP-PT solution exhibited a concentration-dependent photothermal conversion characteristic over time. Specifically, at the same concentration (ICG concentration of 50  $\mu$ g/mL), CIDP-PT was subjected to 808 nm laser irradiation at different power densities (0.5, 1, 1.5, and 2 W/cm<sup>2</sup>) for 600 s (Fig. 2B). The temperature increased with increasing concentration and irradiation time, indicating the excellent PTT of CIDP-PT. This synergistic photothermal conversion capability is conducive to enhancing the efficacy of tumor photothermal therapy. Additionally, the photothermal stability of CIDP-PT was evaluated by subjecting it to five consecutive cycles of laser irradiation (808 nm, 1.5 W/cm<sup>2</sup>). As shown in Fig. 2C, the temperature of the CIDP-PT solution could rise above 45 °C. Unlike the gradual attenuation of photothermal conversion performance observed in ICG, CIDP-PT demonstrated no significant decline in photothermal conversion capability, indicating its remarkable thermal stability and resistance to degradation.

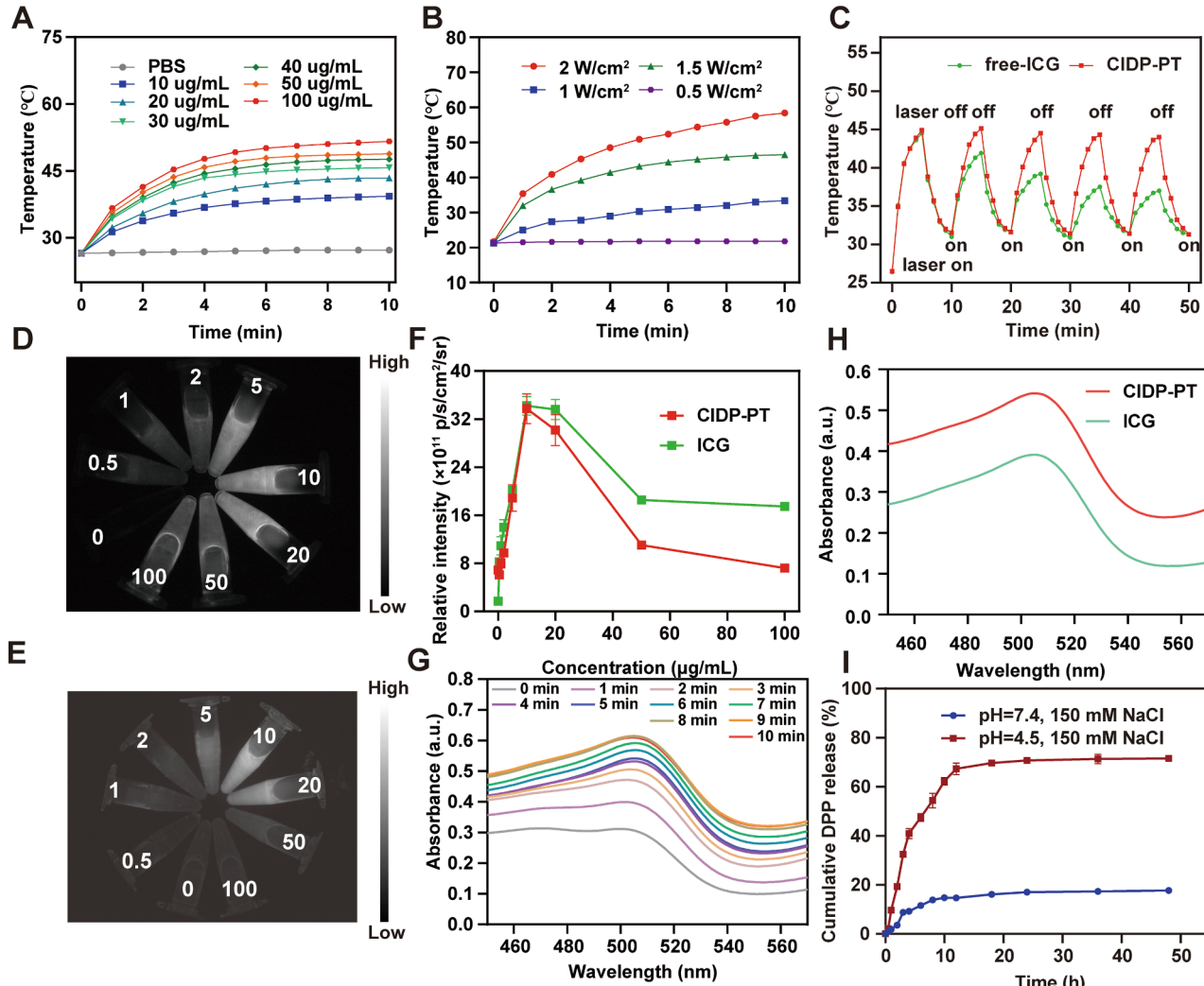


**Fig. 2.** Material characteristics of CIDP-PT (A) Photothermal conversion behavior of CIDP-PT at different concentration (808 nm, 1.5 W/cm<sup>2</sup>); (B) Photothermal conversion behavior of CIDP-PT at different power under 600 s 808 nm laser irradiation (50  $\mu$ g/mL); (C) Temperature change of CIDP-PT and free-ICG for five cycle of laser irradiation (808 nm, 1.5 W/cm<sup>2</sup>); (D) Fluorescence images of CIDP-PT at different concentrations; (E) Fluorescence images of ICG at different concentrations; (F) Quantitative analysis of the fluorescence of CIDP-PT and ICG; (G) SOSG detecting singlet oxygen ( ${}^1\text{O}_2$ ) release ability of CIDP-PT under 808 nm laser irradiation; (H)  ${}^1\text{O}_2$  release ability compared between CIDP-PT and free-ICG; (I) ICP-MS detecting the release curves of DDP in CIDP-PT under acid microenvironment and neutral microenvironment.

One milliliter of CIDP-PT solution at different concentrations (ICG concentrations of 0, 0.5, 1, 2, 5, 10, 20, 50, 100  $\mu\text{g/mL}$ ) was subjected to *in vivo* fluorescence imaging using a small animal imaging system in the near-infrared region (NIR-II). Fluorescence quantification was also performed. It was observed that the fluorescence intensity of CIDP-PT increased with increasing concentration. Below a concentration of 10  $\mu\text{g/mL}$ , the fluorescence intensity exhibited a nearly proportional linear relationship. However, at concentrations above 10  $\mu\text{g/mL}$ , fluorescence quenching occurred. This indicates that CIDP-PT possesses excellent dual-mode imaging capabilities and concentration indication ability. In addition, we took NIR-II fluorescence images of free ICG and obtained similar results to CIDP-PT. It shows that this indication characteristic is given by ICG (Fig. 2D-F). In general, the distribution of CIDP-PT in the body can be visualized using an NIR-II imaging system, making it not only suitable for tumor ablation but also a valuable indicator for drug

distribution.

We utilized SOSG (Singlet Oxygen Sensor Green, provided by Beyotime Biological, China) to assess the singlet oxygen ( ${}^1\text{O}_2$ ) generation capacity of CIDP-PT in an *in vitro* setting. As shown in Fig. 2G, during laser irradiation, CIDP-PT exhibited a single peak at 505 nm, indicating the presence of singlet oxygen. The concentration of  ${}^1\text{O}_2$  increased over time, and no significant change in solution color was observed. Rapid generation of singlet oxygen occurred within the first 0–5 min, followed by a slower release between 5–10 min. After 8 min, the absorption peak remained relatively stable. Further analysis revealed that the increase in absorbance in the CIDP-PT group was faster than that in the free-ICG group, indicating a higher production of singlet oxygen compared to free ICG. This can be attributed to the protective and anti-degradation effects of  $\text{CaCO}_3$  and PEG on ICG, as well as the inherent ability of  $\text{CaCO}_3$  to generate singlet oxygen. These factors

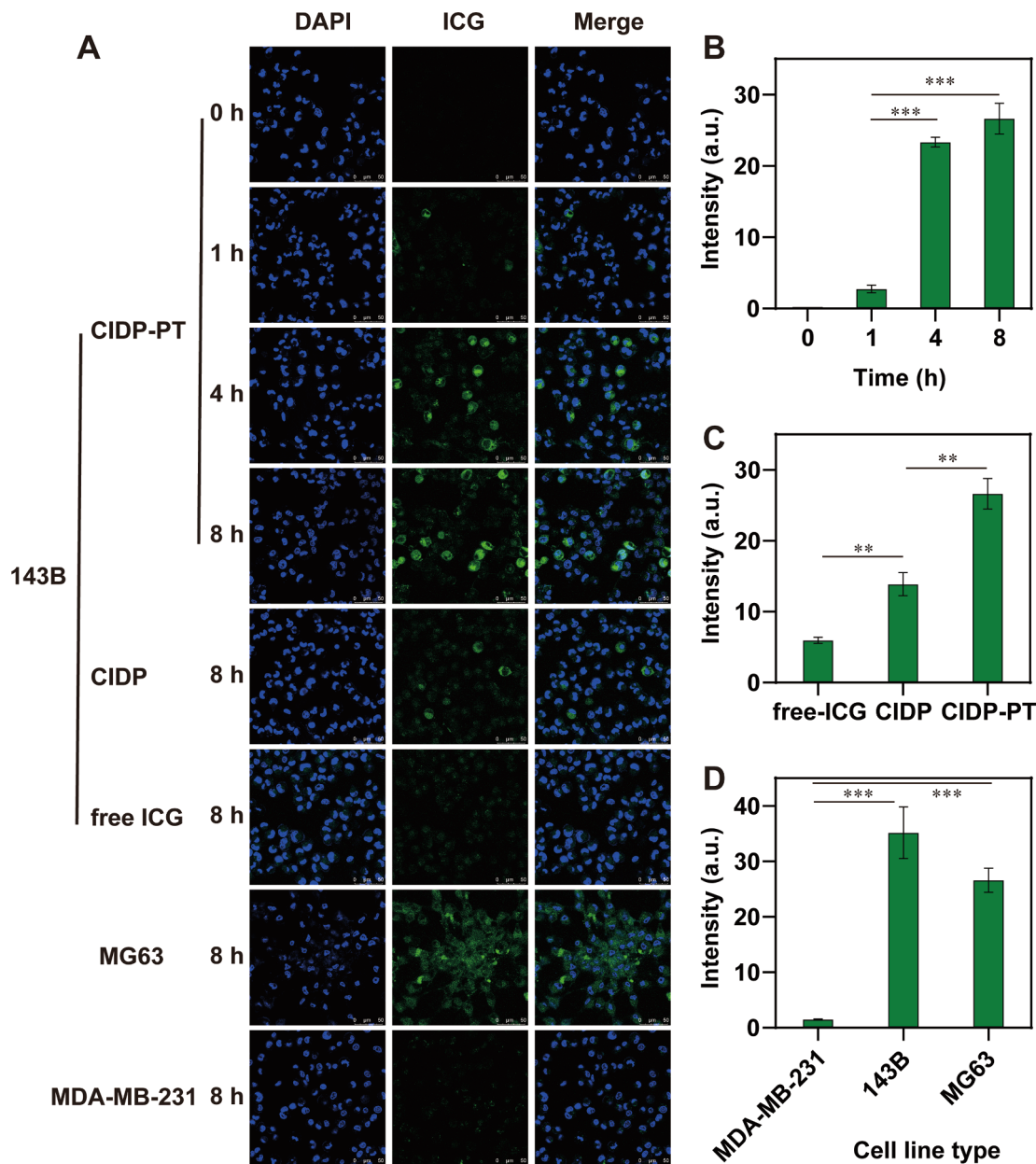


**Fig. 3.** (A) The CLSM images of osteosarcoma cell line 143B + MG63 and breast cancer cell line MDA-MB-231 uptaking free-ICG, CIDP and CIDP-PT for 0, 1, 4, and 8 h (scale bar = 50  $\mu\text{m}$ , 20  $\mu\text{g}\cdot\text{mL}^{-1}$ ); (B) Fluorescence quantification (green fluorescence) was performed to analyze the uptake of CIDP-PT by 143B cells at different times (Mean  $\pm$  SD, n = 3, student's test, \*\*\* $p$  < 0.001, \*\* $p$  < 0.01, \* $p$  < 0.05); (C) Fluorescence quantification was performed to analyze the uptake of free-ICG, CIDP and CIDP-PT by 143B cells; (D) Fluorescence quantification was performed to analyze the uptake of CIDP-PT between 143B, MG63 and MDA-MB-231 cells. (For interpretation of the references to color in this figure legend, the reader is referred to the web version of this article.)

contribute to a more potent tumor-killing effect at the tumor site (Fig. 2H).

We utilized an acid dissolution-vortex-sonication technique to disrupt the nanostructure of CIDP-PT and facilitate drug release for the assessment of its drug loading efficiency. According to our calculations, the drug loading efficiency of DDP in CIDP-PT was determined to be 16.1 %, signifying a notably high encapsulation efficiency. Simultaneously, we investigated the influence of different pH environments on

drug release. Due to the distinct metabolic and growth requirements of tumors compared to normal cells, the tumor microenvironment and intracellular conditions often tend to be acidic, while the biological microenvironment of most normal tissues remains neutral. To simulate the acidic tumor microenvironment, we used acetic acid buffer solution at pH 4.5, while PBS at pH 7.4 was employed to mimic the neutral biological microenvironment of normal organ sites. These conditions were used to evaluate the pH-responsive drug release performance of

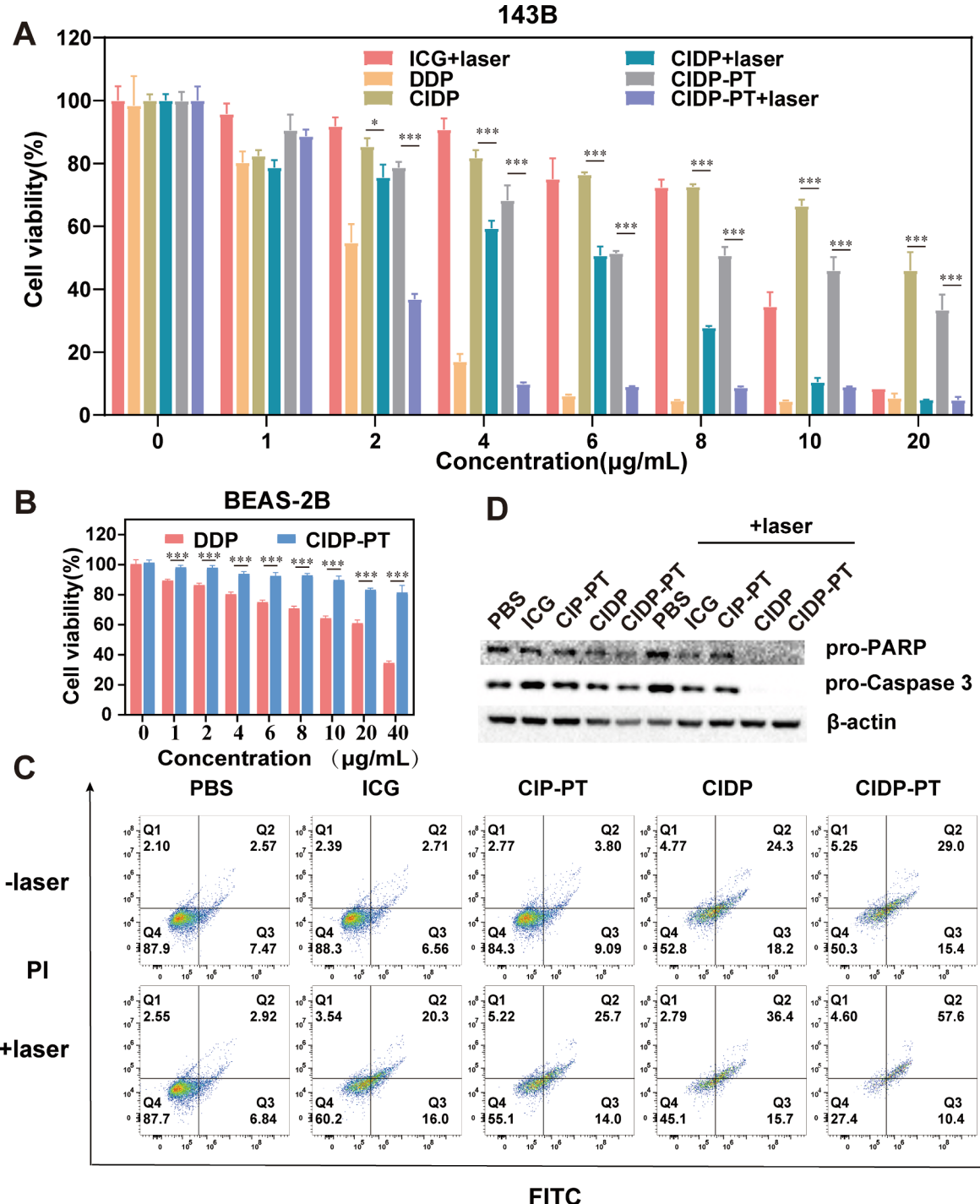


**Fig. 4.** Verification of CIDP-PT in vitro (A) MTT assay for 143B treated with different treatments: ICG + laser, DDP, CIDP, CIDP + laser, CIDP-PT and CIDP-PT + laser at different concentrations, 5 min, 1.5 W/cm<sup>2</sup> (Mean  $\pm$  S.D, n = 3, student's test, \*p < 0.05, \*\*p < 0.01, \*\*\*p < 0.001); (B) MTT assay for normal lung epithelial cells BEAS-2B treated with different treatments: DDP, CIDP-PT at different concentrations, 5 min, 1.5 W/cm<sup>2</sup> (Mean  $\pm$  S.D, n = 3, student's test, \*\*\*p < 0.001); (C) Flow detection of 143B cells apoptosis treating with PBS, ICG, CIP-PT, CIDP and CIDP-PT with laser and without laser (Q4: live cells; Q3: early apoptotic cells; Q2: late apoptotic cells; Q1: dead cells); (D) Western blotting of pro-PARP, pro-Caspase-3 and  $\beta$ -actin expression detecting apoptosis.

CIDP-PT *in vivo*. The cumulative release curves of cisplatin demonstrated significant differences in two distinct pH environments. The cumulative release rate of cisplatin from CIDP-PT at pH 7.4 was  $17.69 \pm 1.03\%$  at 48 h, indicating minimal drug leakage in the microenvironment of normal tissues. However, under pH 4.5 conditions, the cumulative release rate of cisplatin from CIDP-PT increased to  $71.86 \pm 1.21\%$  at 48 h, with a rapid release phase in the first 10 h, which facilitates swift tumor eradication, followed by a sustained release phase to maintain drug concentration at the tumor site (Fig. 2I). Hence, CIDP-PT exhibits pH sensitivity, where under acidic conditions, the decomposition of  $\text{CaCO}_3$  encapsulating cisplatin promotes drug release, enhancing the therapeutic efficacy against tumors. Conversely, under neutral physiological conditions in normal tissues, cisplatin release is minimal, effectively reducing its toxicity to normal tissues.

### 3.3. Cellular uptake of CIDP-PT

As depicted in Fig. 3A-C, the cellular uptake of free FITC-labeled ICG and CIDP-PT was examined in osteosarcoma (143B/MG63) and breast cancer (MDA-MB-231) cells. Confocal laser scanning microscopy (CLSM) images revealed that the green fluorescence intensity of the CIDP-PT incubation group exceeded that of the CIDP group, and both groups exhibited higher intensity compared to the free ICG group. This indicates a higher cellular uptake of CIDP-PT compared to CIDP and free ICG, thus confirming the enhanced active targeting effect of the peptide-based targeting moiety (PT) on osteosarcoma cell uptake of the material. Fluorescence quantification analysis further demonstrated a significant increase in the proportion of FITC-positive cells for CIDP-PT compared to the other two groups. Moreover, as time progressed, the osteosarcoma 143B cells exhibited greater uptake of CIDP-PT, leading to a more pronounced fluorescence intensity. Concurrently, as shown in Fig. 3D, we observed that the fluorescence intensity of the osteosarcoma cell lines MG63 and 143B was significantly higher than that of the breast cancer cell line MDA-MB-231. This finding indicates the specific selectivity of CIDP-PT towards both osteosarcoma cell types from different sources, while further confirming the active targeting effect of the peptide-based targeting moiety (PT) by demonstrating its lack of significant selectivity towards breast cancer tumor cells.

To further investigate the therapeutic potential of CIDP-PT in cellular experiments, the MTT assay was employed to assess its anti-tumor properties. As illustrated in Fig. 4A, following laser irradiation, the CIDP and CIDP-PT groups exhibited superior efficacy in combating tumor growth compared to the non-laser group. Notably, the CIDP-PT + laser group demonstrated even greater effectiveness in inducing cellular cytotoxicity, surpassing the cytotoxicity observed in the other treatment groups. This enhanced effect can be attributed to the combined impact of DDP's inherent cytotoxicity towards 143B cells and CIDP-PT's tumor-targeting properties, resulting in a potentiated tumor eradication. Simultaneously, as depicted in Fig. 4B, CIDP-PT displayed significantly lower cytotoxicity towards normal lung epithelial cells (BEAS-2B) compared to DDP. This observation underscores the favorable biological safety profile of CIDP-PT, as it not only enhances its tumor-killing efficacy but also mitigates the adverse effects associated with the use of cisplatin. These findings provide evidence of CIDP-PT's excellent biocompatibility and reinforce its potential as a safe and effective therapeutic agent for cancer treatment.

To further validate the apoptotic effects of CIDP-PT on 143B cells, the cells were divided into two groups: laser irradiation and non-laser irradiation. The experimental groups included PBS, free ICG, CIP-PT (CIDP-PT without DDP), CIDP, and CIDP-PT, and flow cytometry was performed on the collected cells to assess apoptosis. As shown in Fig. 4C, within the laser irradiation groups, except for the PBS group, all groups treated with laser exhibited a higher percentage of both early and late apoptotic cells compared to the non-laser irradiation group. The CIDP-PT group displayed a higher apoptotic rate than the free-ICG, CIP-PT, and CIDP groups, indicating the significant role of the targeted peptide

PT in enhancing drug accumulation. Furthermore, cisplatin potentiated the induction of cellular apoptosis. This consistent pattern was also observed at the protein level through Western Blot experiments (Fig. 4D). To assess the cellular viability and death status, a live/dead cell viability assay was conducted using a fluorescent reagent. The different treatments resulted in varying fluorescence colors: green for live cells (Calcein-AM) and red for dead cells (PI). Among the groups, including PBS, PBS + laser, free-ICG, and CIP-PT, only green fluorescence was observed, indicating intact cell morphology. However, in the free-ICG + laser, CIP-PT + laser, CIDP, CIDP + laser, CIDP-PT, and CIDP-PT + laser groups, the red fluorescence of the cell nuclei intensified and exhibited a fragmented pattern, indicating significant cell death (Fig. 5A). Quantitative analysis of cell viability (Fig. 5B) showed that the CIDP-PT + laser group had higher fluorescence intensity compared to all other groups, indicating the substantial death of 143B cells under the combined effects of targeted drugs and phototherapy. Fig. 5C and 5D demonstrated that the PBS (control) group and the free-ICG group without laser irradiation showed minimal green fluorescence, indicating negligible ROS generation. In contrast, the ICG + laser, CIDP-PT, and CIDP-PT + laser groups displayed green fluorescence, indicating the generation of ROS in 143B cells upon laser irradiation. The CIDP-PT + laser group exhibited a stronger green fluorescence signal compared to the other groups. This enhancement can be attributed to the PT targeting modification of dry CIDP-PT, which increased its ability to specifically recognize 143B cells, thereby enhancing the cellular uptake of CIDP-PT and subsequent ROS generation under laser irradiation. In addition, the decomposition of calcium carbonate in acidic environments also provides a portion of ROS. These results confirm the *in vitro* anti-tumor effects of CIDP-PT through combined photothermal and photodynamic therapy (PTT/PDT) with targeted drug delivery.

### 3.4. Verification of the extrinsic effects of CIDP-PT

In order to evaluate the impact of CIDP-PT on proliferation, invasion, and migration of osteosarcoma cells, we employed single-agent treatments or combined laser therapy using PBS (control group), ICG, CIDP, and CIDP-PT. As depicted in Fig. 6A, compared to the non-irradiated group, phototherapy resulted in decreased cell migration and proliferation in 143B cells, while CIDP-PT exhibited superior efficacy, significantly reducing the migration distance of 143B cells compared to the other groups. Furthermore, the Transwell assay revealed that CIDP-PT significantly inhibited invasion. The combination of NIR-II laser and CIDP-PT notably enhanced the inhibitory effect of CIDP-PT on the invasion of 143B cells (Fig. 6B, C). Additionally, colony formation assays confirmed that CIDP-PT, after NIR laser treatment, suppressed the clonogenic ability of 143 cells, leading to a marked reduction in the number of formed colonies compared to the control group (Fig. 6D, E).

### 3.5. Verification of the effects of CIDP-PT *in vivo*

To investigate the vascular distribution of CIDP-PT in nude mice, a small amount of CIDP-PT (equivalent to 50  $\mu\text{g}$  ICG) in PBS solution was intravenously injected into tumor-bearing nude mice. As shown in Fig. 7A, using the IVIS imaging system (PerkinElmer, Waltham, MA, USA), we could clearly visualize the vascular pathways and distribution in the mice. Subsequently, we administered ICG and CIDP-PT via tail vein injection in tumor-bearing nude mice at different time points for *in vivo* NIR-II fluorescence imaging to evaluate the targeting specificity of the different agents in osteosarcoma. The experimental results, as depicted in Fig. 7B, demonstrate that CIDP-PT, due to the PT modification, exhibits active targeting towards osteosarcoma in the tumor-bearing nude mice. Additionally, it demonstrates passive targeting due to factors such as particle size and PEG encapsulation. After 4 h of administration, CIDP-PT gradually accumulates in the tumor site, and after 8 h, the fluorescence signal intensity at the tumor site is significantly stronger than in the surrounding tissues. Even after 24 h of

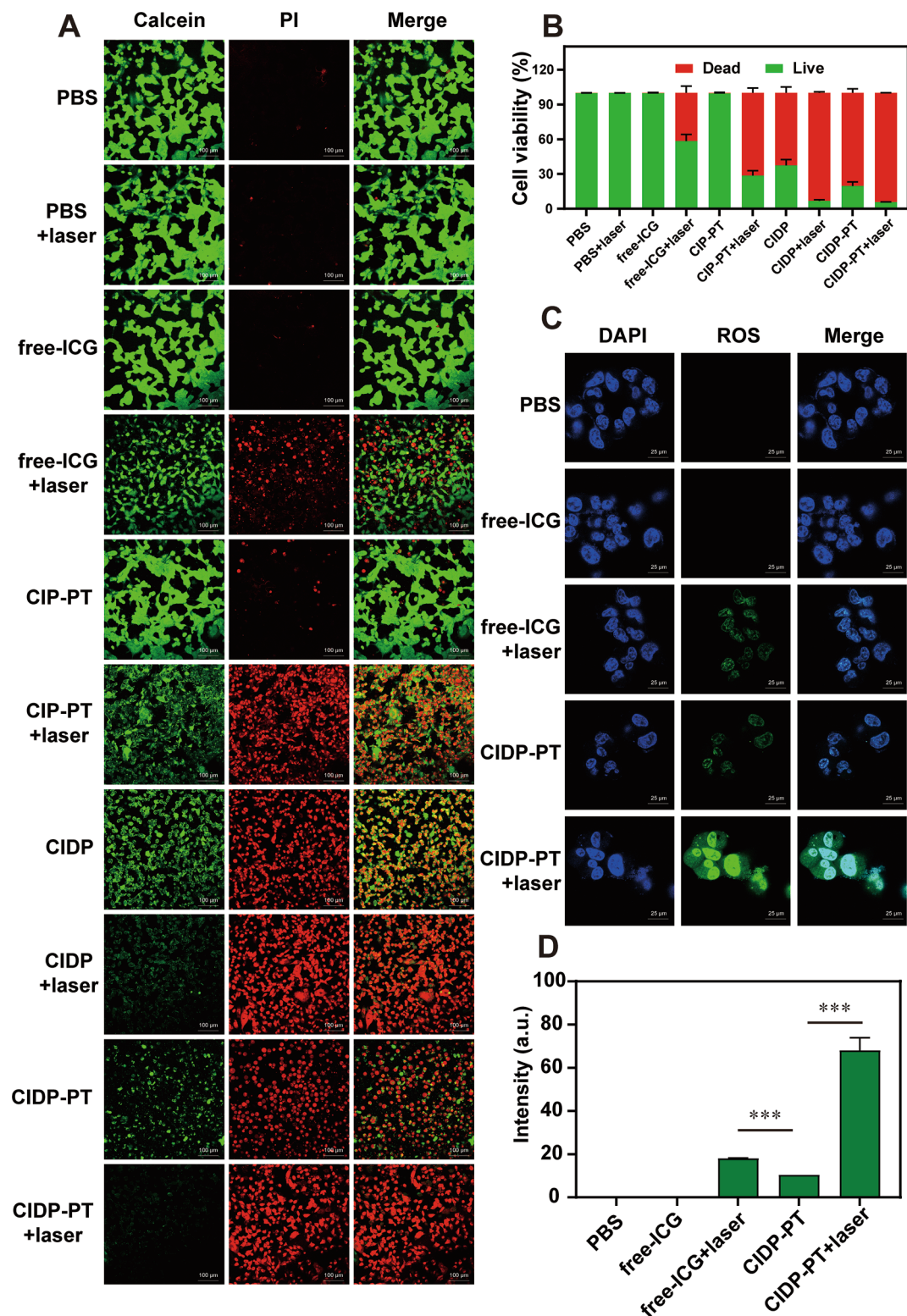


**Fig. 5.** Verification of CIDP-PT in vitro (A) detection of live cells (green) and dead cells (red) in different groups (PBS, free-ICG, CIP-PT, CIDP and CIDP-PT with laser) of confocal microscope (scale bar = 100  $\mu\text{m}$ , 5 min, 1.5  $\text{W}\cdot\text{cm}^{-2}$ , 20  $\mu\text{g}\cdot\text{mL}^{-1}$ ); (B) Fluorescence quantification of live cells and dead cells in different groups; (C) Detection of ROS release in different groups (scale bar = 25  $\mu\text{m}$ , 5 min, 1.5  $\text{W}\cdot\text{cm}^{-2}$ , 20  $\mu\text{g}\cdot\text{mL}^{-1}$ ); (D) Fluorescence quantification of ROS release in different groups (Mean  $\pm$  S.D, n = 3, student's test, \*\*\*p < 0.001). (For interpretation of the references to color in this figure legend, the reader is referred to the web version of this article.)

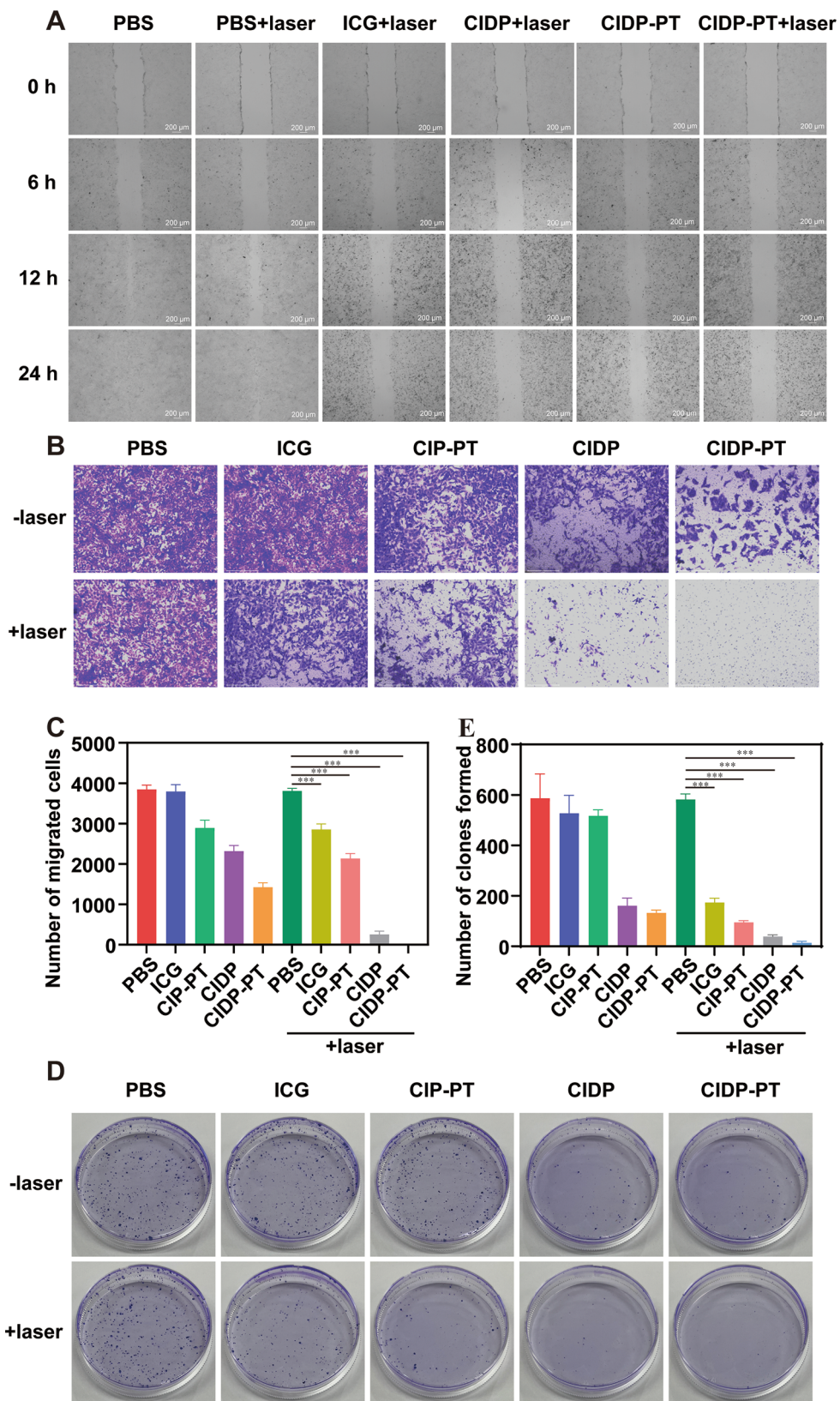


**Fig. 6.** Verification of CIDP-PT in vitro (A) cell migration and proliferation healing experiment detecting inhibition migration of 143B treating with CIDP-PT and other groups after 6, 12, 24 h (scale bar = 200  $\mu$ m); (B) Transwell experiment of 143B treating with CIDP-PT and other groups after 12 h (scale bar = 275  $\mu$ m); (C) Quantitative migration cells (Mean  $\pm$  S.D., n = 3, student's test, \*\*\*p < 0.001); (D) Clonal formation experiment of 143B treating with CIDP-PT and other groups after 2 weeks; (E) Quantitative colony numbers (Mean  $\pm$  S.D., n = 3, student's test, \*\*\*p < 0.001).

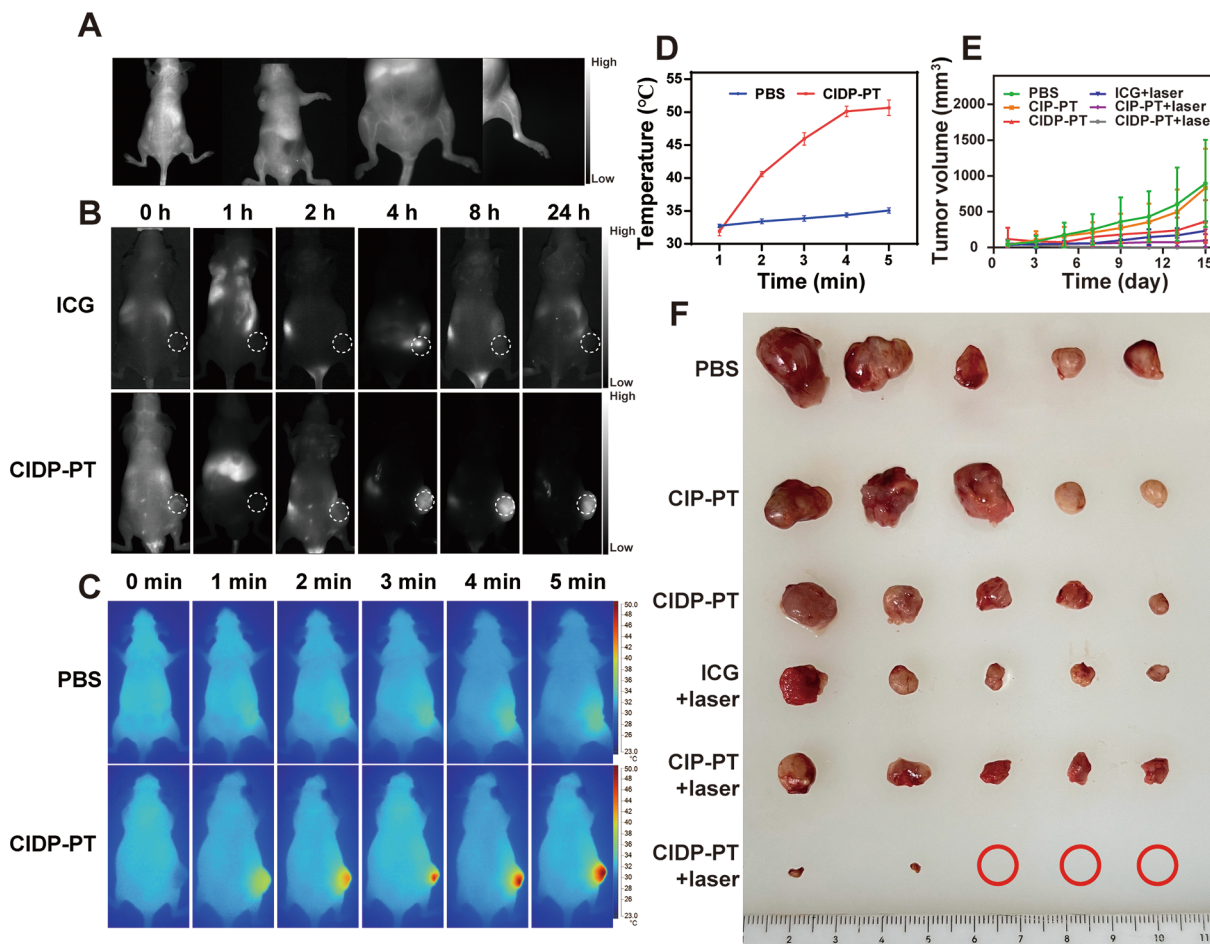


**Fig. 7.** Verification of CIDP-PT in vivo Animal experiment group: (PBS, ICG + laser, CIP-PT, CIP-PT + laser, CIDP, CIDP-PT + laser) (A) IVIS imaging of mouse vascular; (B) In vivo fluorescence images of 143B tumor-bearing mice at 0, 1, 2, 4, 8 and 24 h postadministration of free ICG and CIDP-PT; (C) Thermal images of 143B tumor-bearing mice with intravenous injection of PBS and CIDP-PT; (D) Temperature quantification of thermal imaging; (E) Tumor growth curves of osteosarcoma treated by PBS, ICG, CIP-PT, CIP-PT + laser and CIDP-PT + laser; (F) The volume and image of osteosarcoma after different treatments.

administration, the fluorescence signal remains present at the tumor site. In contrast, in the ICG group, no tumor targeting phenomenon was observed within 24 h. The fluorescence signal diffused throughout the body, gradually accumulating in the kidneys and diminishing over time. After 24 h of administration, the fluorescence of ICG in the body was almost undetectable, indicating that ICG had been largely metabolized. These experimental results are consistent with the cellular uptake results, further confirming the tumor-specific targeting of CIDP-PT and its prolonged retention at the tumor site, thereby exhibiting persistent anti-tumor effects.

Based on the aforementioned experiments, it is evident that the signal intensity of CIDP-PT at the tumor site reaches its peak 8 h after intravenous administration via the tail vein. Therefore, in this experiment, NIR laser irradiation was applied to the tumor-bearing mice 8 h after the administration of CIDP-PT, in order to investigate the in vivo photothermal effect. As shown in Fig. 7C, the evaluation results of in vivo and in vitro photothermal effects are consistent. Following irradiation with an 808 nm laser, there was no significant change in tumor site temperature in the control group, while the CIDP-PT administration group exhibited a rapid increase in temperature at the tumor site, reaching up to 50 °C, which is sufficient to effectively destroy tumor cells (Fig. 7D). These results confirm that CIDP-PT can also generate significant photothermal effects in vivo after light irradiation, making it suitable for in vivo PTT. Simultaneously, during the 15-day treatment period, we measured the changes in tumor volume every day. As shown in Fig. 7E, the tumor volume in the control group continued to increase.

In contrast, mice treated with CIDP-PT without laser irradiation exhibited better inhibition of tumor growth, while the tumors in mice subjected to phototherapy with CIDP-PT gradually regressed, demonstrating a more pronounced inhibitory effect on tumor proliferation. On the 15th day of treatment, the corresponding tumors were excised and photographed, revealing that the CIDP-PT + laser group displayed superior tumor suppression compared to the other groups (Fig. 7F). These results indicate that the combination of CIDP-PT with PDT/PTT therapy has a higher therapeutic efficacy and exhibits superior anti-tumor effects in vivo, making it an effective photothermal and chemical therapeutic agent for the treatment of osteosarcoma.

As shown in Fig. 8A, the body weight-time curves of the tumor-bearing mice in each treatment group were recorded throughout the course of treatment. It can be observed that the body weights of all treatment groups did not significantly differ from those measured in the control group. In order to further investigate the anti-tumor effects at the histological level, tumor tissue sections were stained with H&E for each treatment group. As shown in Fig. 8B, the tumor cells in the PBS group, with and without light exposure, exhibited a well-preserved cellular morphology, without notable histological changes. However, in the CIDP-PT group subjected to light irradiation, nuclear condensation and disorganized cellular arrangement were observed. The histopathological findings were in agreement with the gross tumor inhibition experiment, providing dual perspectives on the superior therapeutic effects of CIDP-PT in vivo. In Fig. 8C, after completion of the treatment process, major organs (heart, liver, spleen, lung, and kidney) were excised from the

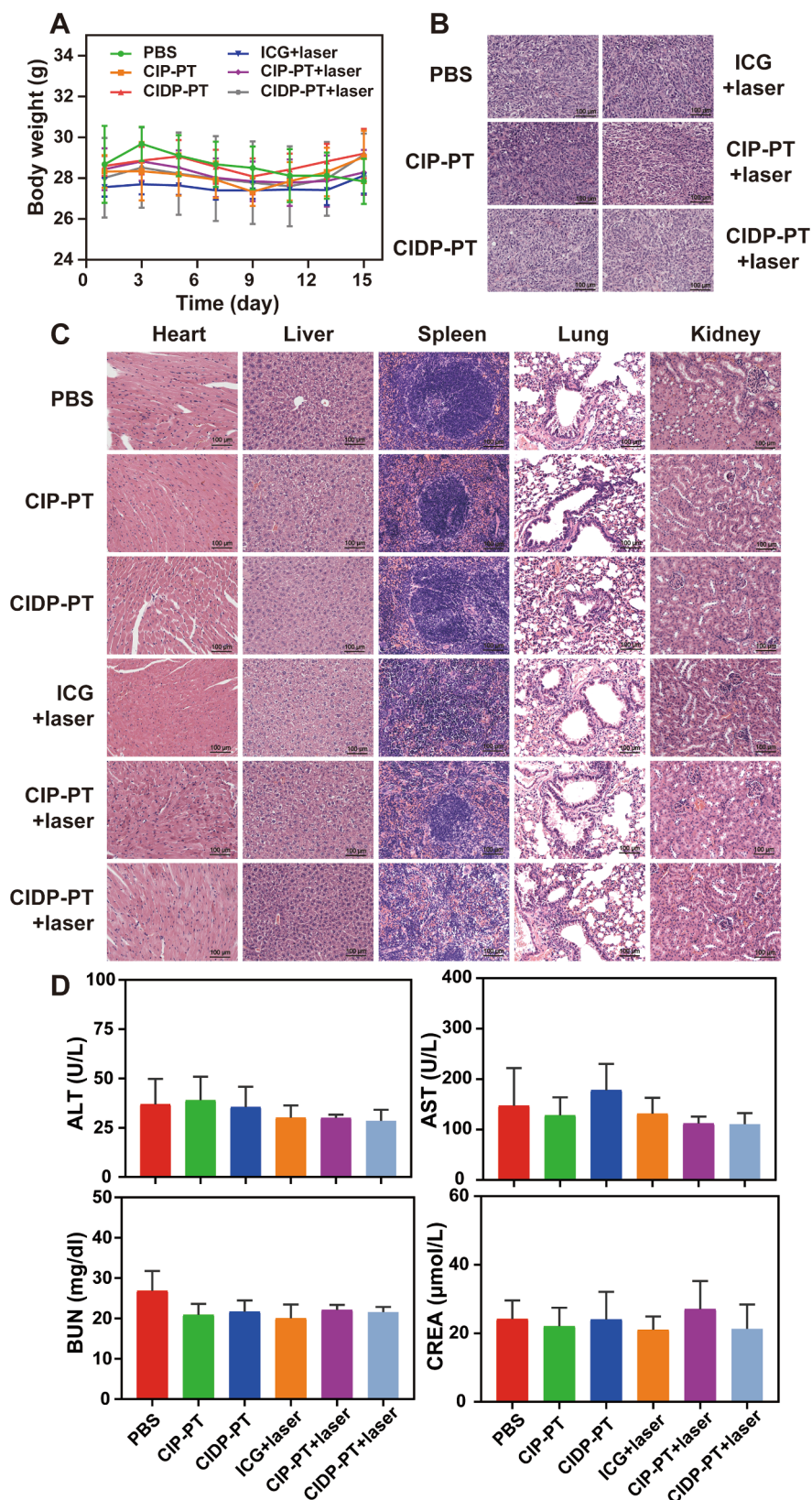


**Fig. 8.** Drug toxicity of CIDP-PT (A) Weight change curves of nude mice bearing tumor under different treatments; (B) Tumor H&E staining photographs of different treatments (scale bar = 100  $\mu$ m); (C) Liver, heart, spleen, kidney and lung H&E staining photographs of different treatments (scale bar = 100  $\mu$ m); (D) Blood biochemistry of liver and kidney function (Mean  $\pm$  S.D., n = 3).

mice of different groups and subjected to hematoxylin and eosin (H&E) staining of tissue sections. No significant histological changes were observed at the tissue level, indicating the absence of structural damage to the major organs and further confirming the biocompatibility of CIDP-PT treatment. Additionally, serum samples collected from the mice after treatment confirmed no significant impairment of liver and kidney function (Fig. 8D). Additionally, on the 15th day post tail vein injection of CIDP-PT and related components, blood samples were collected from the mice to assess routine blood indicators. It was observed that CIDP-PT did not alter the white blood cell count, granulocyte count, red blood cell count, or hemoglobin levels in the mice (Fig. S1). These results confirm the good biocompatibility and safety of CIDP-PT for in vivo treatment.

#### 4. Discussion

In this study, we designed our research based on previous findings that different wavelengths of light therapy can induce varying cellular responses. For instance, red and blue light irradiation have been shown to increase proliferation and osteogenic differentiation of stem cells or induce apoptosis in cancer cells, indicating that cellular responses vary with different wavelength exposures [37–39]. We chose to use near-infrared II (NIR-II) light as the light source for this study. NIR-II light source offers unique advantages compared to other light sources [40]. For example, it exhibits minimal interaction with surrounding tissues, allowing photons to propagate throughout the body with minimal interference. Additionally, NIR-II fluorescence imaging overcomes the penetration/contrast bottleneck of visible light imaging, making it an exceptional approach for early cancer diagnosis and high-sensitivity tumor surgery. Moreover, NIR-II molecular dyes conveniently conjugate with peptides/antibodies, making them ideal candidates for targeted cancer imaging, significantly overcoming the autofluorescence/scattering issues of deep tissue molecular imaging.

Regarding the selection of phototherapy adjuvants, indocyanine green (ICG) has been approved by the U.S. Food and Drug Administration (FDA) for human clinical applications [41]. It possesses reliable therapeutic efficacy and biocompatibility, and emits fluorescence in the NIR-II window, with an emission peak exceeding 1000 nm, making it a good choice for tumor imaging and ablation. However, ICG has limitations such as light sensitivity, rapid clearance and metabolism in the body, and inadequate tumor targeting. Free ICG decomposes rapidly under long-term NIR-II laser irradiation, resulting in short retention time in mice. The ICG-only group exhibits limitations in terms of cellular uptake, MTT assays in tumor cells, apoptosis flow cytometry analysis, and in vivo animal experiments.

The integration of photosensitizing auxiliary materials with nanomaterial drug delivery systems represents a highly promising direction in current research. Specifically, nanomaterial drug delivery systems can concentrate a variety of materials and drugs at specific targets within the body, allowing for enrichment of materials and drugs at the intended site while reducing residual presence in non-target areas. This approach enhances therapeutic effectiveness and addresses the limitations of materials that are prone to degradation and lack strong targeting capabilities. A nanoscale drug delivery system based on nanoparticles can be defined as particles with dimensions ranging from approximately 1 to 1000 nm (with a common diameter of 5 to 350 nm) and can be fabricated using various biocompatible substances. These systems offer advantages in terms of drug bioavailability, serum stability, and pharmacokinetics, thereby significantly improving treatment outcomes. Current research indicates that nanoscale controlled-release formulations provide excellent tissue penetration and allow for slow and controlled release of active ingredients at the target site [42–44]. Scholars have already explored various types of nanoscale drug delivery systems capable of loading multiple drugs, primarily including organic and inorganic materials. Calcium carbonate ( $\text{CaCO}_3$ ) serves as a representative inorganic nanomaterial drug delivery system carrier. The

longer biodegradation time of calcium carbonate and the slow degradation of the  $\text{CaCO}_3$  matrix allow for prolonged retention of drugs after administration. Additionally,  $\text{CaCO}_3$  nanoparticles typically do not expand or alter their porosity in aqueous environments. Moreover,  $\text{CaCO}_3$  exhibits extremely low decomposition probability in the normal physiological environment, but in the acidic environment of tumors, it decomposes to form  $\text{Ca}^{+}$  ions, which interact with ROS, further promoting apoptosis and necrosis of osteosarcoma cells while ensuring stable and timely decomposition. The availability, cost-effectiveness, safety, biocompatibility, pH sensitivity, bone conductivity, and slow biodegradability of calcium carbonate particles make them suitable drug delivery carriers [45–47]. Despite the use of nanoscale calcium carbonate since the early 1990s, there are almost no reports on its hazardous properties, providing additional evidence of the biocompatibility and safety of calcium carbonate [48].

To further enhance the therapeutic efficacy of osteosarcoma treatment, we incorporated cisplatin, the most sensitive chemotherapy drug for osteosarcoma, into our drug delivery system. Cisplatin, discovered by Michele Peyrone in 1845, is one of the most promising and widely used drugs for treating various solid tumors, including testicular, ovarian, head and neck, bladder, lung, cervical, melanoma, and lymphoma [49]. However, side effects and drug resistance present inherent challenges for cisplatin, limiting its application and effectiveness. The main toxicities associated with cisplatin include nephrotoxicity, ototoxicity, hepatotoxicity, gastrointestinal toxicity, and neurotoxicity [50]. In this study, we enhanced the targeting of cisplatin through a nanocarrier system, ensuring maximum therapeutic efficacy while minimizing its biotoxicity. Finally, we validated the reliability of cisplatin release at the tumor site using a simulated tumor acidic microenvironment. We also measured the leakage of CIDP-PT in normal human organs in the control group and found that it remained at a very safe level, with no abnormalities observed in organ structure and function during animal experiments. Compared to using cisplatin alone, the residual presence in non-tumor tissues was significantly reduced, leading to a substantial reduction in toxic side effects.

Furthermore, to improve the water solubility of the calcium carbonate delivery system, we added DSPE-PEG<sub>2000</sub>-COOH to the outer surface of the nanoparticles. DSPE-PEG<sub>2000</sub>-COOH, which stands for 1,2-distearoyl-sn-glycero-3-phosphoethanolamine-polyethylene glycol-carboxylic acid, is a widely used phospholipid-polymer conjugate in drug delivery applications. It is a biocompatible, biodegradable, and amphiphilic material that can be functionalized with various biomolecules to achieve specific functionalities. With the growing interest in using nanocarriers for therapeutic drug delivery and imaging, DSPE-PEG has become a highly useful material for formulating these nanocarriers to achieve prolonged circulation time, improved stability, and enhanced encapsulation efficiency [51–53]. Moreover, we utilized DSPE-PEG<sub>2000</sub>-COOH to provide binding sites for targeting oligopeptides (PT), further enhancing the osteosarcoma-specific active targeting of CIDP-PT and strengthening the anti-tumor properties of the drug. The potent effects of PT in enhancing therapeutic efficacy were observed through MTT assays, apoptosis experiments, cell migration and proliferation experiments, and Transwell assays. In summary, we combined the antitumor effects of phototherapy and chemotherapy in osteosarcoma treatment, harnessing the advantages of both approaches. By utilizing inorganic and organic nanocarrier platforms, we addressed the respective limitations of photosensitizers and chemotherapy drugs, maximized nanoparticle performance, and minimized drug side effects. Satisfactory treatment outcomes were achieved both *invitro* and *in vivo*. It is noteworthy that scientists have increasingly recognized the potential significance of intratumoral antibacterial control in tumors and the regulation of osteogenic properties of tumor cells in the treatment of osteosarcoma. This discovery may mark a new direction in the fight against osteosarcoma [29,30,54]. Ans it is likely to become a new focus of detailed research for our team.

## 5. Conclusion

In summary, a CIDP-PT nanocarrier system was designed and developed for effective therapy of osteosarcoma. In vitro, significant killing and growth inhibition effects of osteosarcoma have been achieved by combining phototherapy and chemotherapy. In vivo experiments showed that the CIDP-PT nanocarrier system significantly reduced the tumor volume in vivo and greatly reduced the tumor burden of mice. Furthermore, the study confirmed the system's excellent biocompatibility and safety profile. Low degree of tissue damage and blood safety make the subsequent clinical transformation possible. In the future clinical treatment of osteosarcoma, CIDP-PT nanocarrier system can integrate superior treatment experience. Presents an efficient treatment effect to patients.

## 6. Declaration of Generative AI and AI-assisted technologies in the writing process

During the preparation of this work the authors did not use AI and AI-assisted technologies. The authors reviewed and edited the content as needed and take full responsibility for the content of the publication.

## CRediT authorship contribution statement

**Li-chen Ji:** Investigation, Writing – original draft. **Jia-qing Huang:** Conceptualization, Investigation, Writing – review & editing. **Xu-gang Zhong:** Writing – review & editing. **Long-cai Liu:** Supervision. **Qi-hong Sun:** Investigation, Formal analysis. **Yong Fan:** Investigation, Formal analysis. **Li Yin:** Investigation. **Qing Bi:** Funding acquisition, Resources. **Qiong Zhang:** Investigation, Formal analysis. **Yu Cai:** Investigation, Writing – original draft. **Ze-ju He:** Writing – original draft.

## Declaration of competing interest

The authors declare the following financial interests/personal relationships which may be considered as potential competing interests: Zeju He reports was provided by Zhejiang Provincial People's Hospital. Zeju He reports a relationship with Zhejiang Provincial People's Hospital that includes: employment. If there are other authors, they declare that they have no known competing financial interests or personal relationships that could have appeared to influence the work reported in this paper.

## Data availability

Data will be made available on request.

## Acknowledgement

This work was supported by grants from Basic Public Welfare Research Program of Zhejiang Province (LGF22H060029), National Science Foundation China (Grant No. 81672769).

## Appendix A. Supplementary data

Supplementary data to this article can be found online at <https://doi.org/10.1016/j.matdes.2024.112965>.

## References

- [1] J.J. Morrow, I. Bayles, A.P.W. Funnell, T.E. Miller, A. Saiakhova, M.M. Lizardo, C. F. Bartels, M.Y. Kapteijn, S. Hung, A. Mendoza, G. Dhillon, D.R. Chee, J.T. Myers, F. Allen, M. Gambarotti, A. Righi, A. DiFeo, B.P. Rubin, A.Y. Huang, P.S. Meltzer, L. J. Helman, P. Picci, H.H. Versteeg, J.A. Stamatoyannopoulos, C. Khanna, P. C. Scacheri, Positively selected enhancer elements endow osteosarcoma cells with metastatic competence, *Nat. Med.* 24 (2) (2018) 176–185, <https://doi.org/10.1038/nm.4475>.
- [2] M.F. Hansen, M. Seton, A. Merchant, Osteosarcoma in Paget's disease of bone, *J. Bone Miner. Res.* 21 (Suppl 2) (2006) P58–P63, <https://doi.org/10.1359/jbmr.06s211>.
- [3] Z. Shoaib, T.M. Fan, J.M.K. Irudayraj, Osteosarcoma mechanobiology and therapeutic targets, *Br. J. Pharmacol.* 179 (2) (2022) 201–217, <https://doi.org/10.1111/bph.15713>.
- [4] H.C. Beird, S.S. Bielack, A.M. Flanagan, J. Gill, D. Heymann, K.A. Janeway, J. A. Livingston, R.D. Roberts, S.J. Strauss, R. Gorlick, Osteosarcoma, *Nat. Rev. Dis. Primers* 8 (1) (2022) 77, <https://doi.org/10.1038/s41572-022-00409-y>.
- [5] K.L. Huang, C.F. Chen, P.K. Wu, P.C. Chen, W.M. Chen, C.L. Liu, T.H. Chen, Clinical outcomes and prognostic factors of Ewing sarcoma: a clinical analysis of 12 patients in Taiwan, *J. Chin. Med. Assoc.* 75 (1) (2012) 16–20, <https://doi.org/10.1016/j.jcma.2011.10.013>.
- [6] L. Ren, A. Mendoza, J. Zhu, J.W. Briggs, C. Halsey, E.S. Hong, S.S. Burkett, J. Morrow, M.M. Lizardo, T. Osborne, S.Q. Li, H.H. Luu, P. Meltzer, C. Khanna, Characterization of the metastatic phenotype of a panel of established osteosarcoma cells, *Oncotarget* 6 (30) (2015) 29469–29481, <https://doi.org/10.18632/oncotarget.5177>.
- [7] J.L. Ferguson, S.P. Turner, Bone cancer: diagnosis and treatment principles, *Am. Fam. Physician* 98 (4) (2018) 205–213.
- [8] N.M. Bernthal, N. Federman, F.R. Eilber, S.D. Nelson, J.J. Eckardt, F.C. Eilber, W. D. Tap, Long-term results (>25 years) of a randomized, prospective clinical trial evaluating chemotherapy in patients with high-grade, operable osteosarcoma, *Cancer* 118 (23) (2012) 5888–5893, <https://doi.org/10.1002/cncr.27651>.
- [9] C. Chen, L. Xie, T. Ren, Y. Huang, J. Xu, W. Guo, Immunotherapy for osteosarcoma: Fundamental mechanism, rationale, and recent breakthroughs, *Cancer Lett.* 500 (2021) 1–10, <https://doi.org/10.1016/j.canlet.2020.12.024>.
- [10] M. Anderson, Update on Survival in Osteosarcoma, *Orthop. Clin. North Am.* 47 (1) (2016) 283–292, <https://doi.org/10.1016/j.ocl.2015.08.022>.
- [11] D.R. Reed, M. Hayashi, L. Wagner, O. Binitie, D.A. Steppan, A.S. Brohl, E. T. Shinohara, J.A. Bridge, D.M. Loeb, S.C. Borinstein, M.S. Isakoff, Treatment pathway of bone sarcoma in children, adolescents, and young adults, *Cancer* 123 (12) (2017) 2206–2218, <https://doi.org/10.1002/cncr.30589>.
- [12] E. Rothzberg, A.L. Pfaff, S. Koks, Innovative approaches for treatment of osteosarcoma, *Exp. Biol. Med. (Maywood)* 247 (4) (2022) 310–316, <https://doi.org/10.1177/15353702211067718>.
- [13] B. Moukengue, M. Lallier, M. Marchandet, M. Baud'huin, F. Verrecchia, B. Ory, F. Lamoureux, Origin and therapies of osteosarcoma, *Cancers (Basel)* 14 (14) (2022), <https://doi.org/10.3390/cancers14143503>.
- [14] Y. Zhang, J. Yang, N. Zhao, C. Wang, S. Kamar, Y. Zhou, Z. He, J. Yang, B. Sun, X. Shi, L. Han, Z. Yang, Progress in the chemotherapeutic treatment of osteosarcoma, *Oncol. Lett.* 16 (5) (2018) 6228–6237, <https://doi.org/10.3892/ol.2018.9434>.
- [15] J. Yin, S. Pan, X. Guo, Y. Gao, D. Zhu, Q. Yang, J. Gao, C. Zhang, Y. Chen, Nb(2)C MXene-functionalized scaffolds enables osteosarcoma phototherapy and angiogenesis/osteogenesis of bone defects, *Nanomicro Lett* 13 (1) (2021) 30, <https://doi.org/10.1007/s40820-020-00547-6>.
- [16] J. Sun, F. Xing, J. Braun, F. Traub, P.M. Rommens, Z. Xiang, U. Ritz, Progress of phototherapy applications in the treatment of bone cancer, *Int. J. Mol. Sci.* 22 (21) (2021), <https://doi.org/10.3390/ijms22111354>.
- [17] C.M. Au, S.K. Luk, C.J. Jackson, H.K. Ng, C.M. Yow, S.S. To, Differential effects of photofrin, 5-aminolevulinic acid and calphostin C on glioma cells, *J. Photochem. Photobiol. B* 85 (2) (2006) 92–101, <https://doi.org/10.1016/j.jphotobiol.2006.06.002>.
- [18] W. Gu, T. Zhang, J. Gao, Y. Wang, D. Li, Z. Zhao, B. Jiang, Z. Dong, H. Liu, Albumin-bioinspired iridium oxide nanoplateform with high photothermal conversion efficiency for synergistic chemo-photothermal of osteosarcoma, *Drug Deliv.* 26 (1) (2019) 918–927, <https://doi.org/10.1080/10717544.2019.1662513>.
- [19] E.A. Dick, R. Joarder, M.G. De Jode, P. Wragg, J.A. Vale, W.M. Gedroyc, Magnetic resonance imaging-guided laser thermal ablation of renal tumours, *BJU Int.* 90 (9) (2002) 814–822, <https://doi.org/10.1046/j.1464-410x.2002.03026.x>.
- [20] T.J. Vogl, V. Freier, N.E. Nour-Eldin, K. Eichler, S. Zangos, N.N. Naguib, Magnetic resonance-guided laser-induced interstitial thermotherapy of breast cancer liver metastases and other noncolorectal cancer liver metastases: an analysis of prognostic factors for long-term survival and progression-free survival, *Invest. Radiol.* 48 (6) (2013) 406–412, <https://doi.org/10.1097/RLI.0b013e31828328d7>.
- [21] J.P. Ritz, K.S. Lehmann, U. Zurbuchen, F. Wacker, F. Brehm, C. Isbert, C.T. Germer, H.J. Buhr, C. Holmer, Improving laser-induced thermotherapy of liver metastases—effects of arterial microembolization and complete blood flow occlusion, *Eur. J. Surg. Oncol.* 33 (5) (2007) 608–615, <https://doi.org/10.1016/j.ejso.2007.02.028>.
- [22] H.O. Beisland, S. Sander, E. Fossberg, Neodymium:YAG laser irradiation of urinary bladder tumors. Follow-up study of 100 consecutively treated patients, *Urology* 25 (6) (1985) 559–563, [https://doi.org/10.1016/0090-4295\(85\)90279-1](https://doi.org/10.1016/0090-4295(85)90279-1).
- [23] H.J. Schwarzenmaier, F. Eickmeyer, W. von Tempelhoff, V.U. Fiedler, H. Niehoff, S. D. Ulrich, Q. Yang, F. Ulrich, MR-guided laser-induced interstitial thermotherapy of recurrent glioblastoma multiforme: preliminary results in 16 patients, *Eur. J. Radiol.* 59 (2) (2006) 208–215, <https://doi.org/10.1016/j.ejrad.2006.05.010>.
- [24] D. Dolmans, A. Kadambi, J. Hill, K. Flores, J. Gerber, J. Walker, I. Borel Rinkes, R. Jain, D. Fukumura, Targeting tumor vasculature and cancer cells in orthotopic breast tumor by fractionated photosensitizer dosing photodynamic therapy, *Cancer Res.* 62 (15) (2002) 4289–4294.
- [25] H. Cheng, D. Huo, C. Zhu, S. Shen, W. Wang, H. Li, Z. Zhu, Y. Xia, Combination cancer treatment through photothermally controlled release of selenous acid from gold nanocages, *Biomaterials* 178 (2018) 517–526, <https://doi.org/10.1016/j.biomaterials.2018.03.058>.

- [26] L. Feng, Y. Liu, Y. Chen, Q. Xiang, Y. Huang, Z. Liu, W. Xue, R. Guo, Injectable antibacterial hydrogel with asiaticoside-loaded liposomes and ultrafine silver nanosilver particles promotes healing of burn-infected wounds, *Adv. Healthc. Mater.* 12 (22) (2023) e2203201.
- [27] N. Yu, Z. Wang, J. Zhang, Z. Liu, B. Zhu, J. Yu, M. Zhu, C. Peng, Z. Chen, Thiol-capped Bi nanoparticles as stable and all-in-one type theranostic nanoagents for tumor imaging and thermoradiotherapy, *Biomaterials* 161 (2018) 279–291, <https://doi.org/10.1016/j.biomaterials.2018.01.047>.
- [28] W. Sun, C. Qian, L. Wang, M. Wei, M.L. Mastronardi, G. Casillas, J. Breu, G.A. Ozin, Switching-on quantum size effects in silicon nanocrystals, *Adv. Mater.* 27 (4) (2015) 746–749, <https://doi.org/10.1002/adma.201403552>.
- [29] H. Cheng, M. Zhang, H. Hu, Z. Gong, Y. Zeng, J. Chen, Z. Zhu, Y. Wan, Selenium-Modified TiO<sub>2</sub> Nanoarrays with Antibacterial and Anticancer Properties for Postoperation Therapy Applications, *ACS Appl Bio Mater* 1 (5) (2018) 1656–1666, <https://doi.org/10.1021/acsbm.8b00486>.
- [30] H. Cheng, L. Mao, X. Xu, Y. Zeng, D. Lan, H. Hu, X. Wu, H. You, X. Yang, R. Li, Z. Zhu, The bifunctional regulation of interconnected Zn-incorporated ZrO<sub>2</sub> nanoarrays in antibiosis and osteogenesis, *Biomater. Sci.* 3 (4) (2015) 665–680, <https://doi.org/10.1039/c4bm00263f>.
- [31] X. Wang, G. Ku, M.A. Wegiel, D.J. Bornhop, G. Stoica, L.V. Wang, Noninvasive photoacoustic angiography of animal brains in vivo with near-infrared light and an optical contrast agent, *Opt. Lett.* 29 (7) (2004) 730–732, <https://doi.org/10.1364/ol.29.000730>.
- [32] Y.-W. Wang, Y.-Y. Fu, Q. Peng, S.-S. Guo, G. Liu, J. Li, H.-H. Yang, G.-N. Chen, Dye-enhanced graphene oxide for photothermal therapy and photoacoustic imaging, *J. Mater. Chem. B* 1 (42) (2013) 5762–5767.
- [33] W.S. Kuo, Y.T. Chang, K.C. Cho, K.C. Chiu, C.H. Lien, C.S. Yeh, S.J. Chen, Gold nanomaterials conjugated with indocyanine green for dual-modality photodynamic and photothermal therapy, *Biomaterials* 33 (11) (2012) 3270–3278, <https://doi.org/10.1016/j.biomaterials.2012.01.035>.
- [34] M.A. Yaseen, J. Yu, B. Jung, M.S. Wong, B. Anvari, Biodistribution of encapsulated indocyanine green in healthy mice, *Mol. Pharm.* 6 (5) (2009) 1321–1332, <https://doi.org/10.1021/mp800270t>.
- [35] A. Ashokan, G.S. Gowd, V.H. Somasundaram, A. Bhupathi, R. Peethambaran, A. K. Unni, S. Palaniswamy, S.V. Nair, M. Koyakutty, Multifunctional calcium phosphate nano-contrast agent for combined nuclear, magnetic and near-infrared in vivo imaging, *Biomaterials* 34 (29) (2013) 7143–7157, <https://doi.org/10.1016/j.biomaterials.2013.05.077>.
- [36] Y. Yuan, S. Diao, X. Ni, D. Zhang, W. Yi, C. Jian, X. Hu, D. Li, A. Yu, W. Zhou, Q. Fan, Peptide-based semiconducting polymer nanoparticles for osteosarcoma-targeted NIR-II fluorescence/NIR-I photoacoustic dual-model imaging and photothermal/photodynamic therapies, *J. Nanobiotechnol.* 20 (1) (2022) 44, <https://doi.org/10.1186/s12951-022-01249-4>.
- [37] T. Asai, H. Suzuki, M. Kitayama, K. Matsumoto, A. Kimoto, M. Shigeoka, T. Komori, The long-term effects of red light-emitting diode irradiation on the proliferation and differentiation of osteoblast-like MC3T3-E1 cells, *Kobe J. Med. Sci.* 60 (1) (2014) E12–E18.
- [38] P.S. Oh, K.S. Na, H. Hwang, H.S. Jeong, S. Lim, M.H. Sohn, H.J. Jeong, Effect of blue light emitting diodes on melanoma cells: involvement of apoptotic signaling, *J. Photochem. Photobiol. B* 142 (2015) 197–203, <https://doi.org/10.1016/j.jphotobiol.2014.12.006>.
- [39] T. Yoshimoto, Y. Morine, C. Takasu, R. Feng, T. Ikemoto, K. Yoshikawa, S. Iwahashi, Y. Saito, H. Kashihara, M. Akutagawa, T. Emoto, Y. Kinouchi, M. Shimada, Blue light-emitting diodes induce autophagy in colon cancer cells by Opsin 3, *Ann Gastroenterol Surg* 2 (2) (2018) 154–161, <https://doi.org/10.1002/agrs.12055>.
- [40] S. Zhu, R. Tian, A.L. Antaris, X. Chen, H. Dai, Near-infrared-II molecular dyes for cancer imaging and surgery, *Adv. Mater.* 31 (24) (2019) e1900321.
- [41] L. Boni, G. David, A. Mangano, G. Dionigi, S. Rausei, S. Spampatti, E. Cassinotti, A. Fingerhut, Clinical applications of indocyanine green (ICG) enhanced fluorescence in laparoscopic surgery, *Surg. Endosc.* 29 (7) (2015) 2046–2055, <https://doi.org/10.1007/s00464-014-3895-x>.
- [42] S.M. Dizaj, F. Lotfipour, M. Barzegar-Jalali, M.H. Zarrintan, K. Adibkia, Antimicrobial activity of the metals and metal oxide nanoparticles, *Mater Sci Eng C Mater Biol Appl* 44 (2014) 278–284, <https://doi.org/10.1016/j.msec.2014.08.031>.
- [43] M.N. Ravi Kumar, Nano and microparticles as controlled drug delivery devices, *J. Pharm. Pharm. Sci.* 3 (2) (2000) 234–258.
- [44] M.E. Akerman, W.C. Chan, P. Laakkonen, S.N. Bhatia, E. Ruoslahti, Nanocrystal targeting in vivo, *PNAS* 99 (20) (2002) 12617–12621, <https://doi.org/10.1073/pnas.152463399>.
- [45] C. Zhou, T. Chen, C. Wu, G. Zhu, L. Qiu, C. Cui, W. Hou, W. Tan, Aptamer CaCO<sub>3</sub> nanostructures: a facile, pH-responsive, specific platform for targeted anticancer theranostics, *Chem. Asian J.* 10 (1) (2015) 166–171, <https://doi.org/10.1002/asia.201403115>.
- [46] H. Ohgushi, M. Okumura, T. Yoshikawa, K. Inoue, N. Senpuku, S. Tamai, E. C. Shors, Bone formation process in porous calcium carbonate and hydroxyapatite, *J. Biomed. Mater. Res.* 26 (7) (1992) 885–895, <https://doi.org/10.1002/jbm.820260705>.
- [47] S. Huang, J.C. Chen, C.W. Hsu, W.H. Chang, Effects of nano calcium carbonate and nano calcium citrate on toxicity in ICR mice and on bone mineral density in an ovariectomized mice model, *Nanotechnology* 20 (37) (2009) 375102, <https://doi.org/10.1088/0957-4484/20/37/375102>.
- [48] S. Biradar, P. Ravichandran, R. Gopikrishnan, V. Goornavar, J.C. Hall, V. Ramesh, S. Baluchamy, R.B. Jeffers, G.T. Ramesh, Calcium carbonate nanoparticles: synthesis, characterization and biocompatibility, *J. Nanosci. Nanotechnol.* 11 (8) (2011) 6868–6874, <https://doi.org/10.1166/jnn.2011.4251>.
- [49] S. Ghosh, Cisplatin: The first metal based anticancer drug, *Bioorg. Chem.* 88 (2019) 102925, <https://doi.org/10.1016/j.bioorg.2019.102925>.
- [50] L. Astolfi, S. Ghiselli, V. Guarani, M. Chicca, E. Simoni, E. Olivetto, G. Lelli, A. Martini, Correlation of adverse effects of cisplatin administration in patients affected by solid tumours: a retrospective evaluation, *Oncol. Rep.* 29 (4) (2013) 1285–1292, <https://doi.org/10.3892/or.2013.2279>.
- [51] C. Delgado, G.E. Francis, D. Fisher, The uses and properties of PEG-linked proteins, *Crit. Rev. Ther. Drug Carrier Syst.* 9 (3–4) (1992) 249–304.
- [52] D. Needham, T.J. McIntosh, D.D. Lasic, Repulsive interactions and mechanical stability of polymer-grafted lipid membranes, *Biochim. Biophys. Acta* 1108 (1) (1992) 40–48, [https://doi.org/10.1016/0005-2736\(92\)90112-y](https://doi.org/10.1016/0005-2736(92)90112-y).
- [53] V.P. Torchilin, V.G. Omelyanenko, M.I. Papisov, A.A. Bogdanov Jr., V. S. Trubetskoy, J.N. Herron, C.A. Gentry, Poly(ethylene glycol) on the liposome surface: on the mechanism of polymer-coated liposome longevity, *Biochim. Biophys. Acta* 1195 (1) (1994) 11–20, [https://doi.org/10.1016/0005-2736\(94\)90003-5](https://doi.org/10.1016/0005-2736(94)90003-5).
- [54] M. Zhang, J. Zhang, J. Chen, Y. Zeng, Z. Zhu, Y. Wan, Fabrication of curcumin-modified TiO<sub>2</sub> nanoarrays via cyclodextrin based polymer functional coatings for osteosarcoma therapy, *Adv. Healthc. Mater.* 8 (23) (2019) e1901031.